Research Square

Preprints are preliminary reports that have not undergone peer review.
They should not be considered conclusive, used to inform clinical practice,
or referenced by the media as validated information.

Green Synthesis and Defect-State Investigation of Cerium Oxide Nanoparticles via Anogeissus latifolia Bark Extract: Insights into Photocatalytic and Antimicrobial Study

Swapnil H. Susundre
Hislop College, RTM Nagpur University
Swapnil R. Mouje
Hislop College, RTM Nagpur University
Harshal S. Bhoyar
Ramdeobaba University
Mayur V. Khedkar
Hislop College, RTM Nagpur University
Shoeb R. Khan
shoebrk@gmail.com

Hislop College, RTM Nagpur University

Research Article

Keywords: Anogeissus latifolia, Cerium oxide nanoparticles, Photoluminescence, Rhodamine B, Antibacterial activity, Antifungal activity, Photocatalytic degradation

Posted Date: November 3rd, 2026

DOI: https://doi.org/10.21203/rs.3.rs-11578363/v1

License: This work is licensed under a Creative Commons Attribution 4.0 International License.
Read Full License

Additional Declarations: No competing interests reported.

Green Synthesis and Defect-State Investigation of Cerium Oxide Nanoparticles via *Anogeissus latifolia* Bark Extract: Insights into Photocatalytic and Antimicrobial Study

Swapnil H. Susundre[1], *Swapnil R. Mouje*[1],
Harshal S. Bhoyar[2], *Mayur V. Khedkar*[1], *Shoeb R. Khan**[1]
[1]PG and Research Department of Chemistry, Hislop College,
RTM Nagpur University, Nagpur, 440001, Maharashtra, India
[2]Department of Physics, Ramdeobaba University, Nagpur, 440013,
Maharashtra, India
Email: shoebrk@gmail.com

Abstract:

In the present study, a simple, eco-friendly, and cost-effective biogenic route was developed for the synthesis of cerium oxide nanoparticles using the aqueous bark extract of *Anogeissus latifolia* (Dhawada-D) functioning simultaneously as a bio-reducing, caping, and stabilizing agent. Cerous nitrate hexahydrate served as the metal precursor. The biosynthesized cerium oxide nanoparticles were thoroughly characterized using X-ray diffraction, Fourier transform infrared spectroscopy, ultraviolet-visible-near infrared spectroscopy, photoluminescence spectroscopy, scanning electron microscopy with energy-dispersive X-ray spectroscopy, high-resolution transmission electron microscopy and selected area electron diffraction and thermogravimetric analysis techniques. The cerium oxide nanoparticles displayed outstanding multifunctional performance they acted as an efficient heterogeneous photocatalytic for the degradation of Rhodamine B dye under light irradiation and it showed significant antibacterial potential for *Escherichia coli* and *Staphylococcus aureus*, as well as antifungal activity against the *Aspergillus nigher* and *Candida albicans* were studied. These results underscore the potential of biosynthesized cerium oxide nanoparticles in wastewater remediation, optoelectronics, pharmaceutical and biomedical applications, highlighting the promise of green synthesis strategies in nanomaterial development.

Keywords: *Anogeissus latifolia*, Cerium oxide nanoparticles, Photoluminescence, Rhodamine B, Antibacterial activity, Antifungal activity, Photocatalytic degradation

1. Introduction

In recent years, nanotechnology is considered to be a multidisciplinary area at the boundary between chemistry, physics, biology, and materials science, which involves creation

and implantation of nano materials, whose size usually varies from 1 to 100 nm [1-3]. Nano materials have unique physiochemical properties, which differ greatly from those of bulk materials due to such factors as high surface area to volume ratio, quantum effects, and changes in surface electronic structure [4]. Chemically speaking, this affects the materials surface energy, adsorption, redox activity, catalytic properties, and interaction with other molecules [5]. Nanotechnology thus attracts much attention in relation to its use in catalysis, environmental cleanup, chemical sensing, energy generation, and medicine [6]. Metal oxide nanoparticles are of particular interest among different types of nanomaterials because their composition, crystal structure, morphology, and surface properties can be controlled to attain the desired functionality [7].

Metal oxide nanoparticles such as CuO, ZnO, TiO_2, Fe_3O_4, and CeO_2 have been studied in great detail due to their unique chemical, optical, catalytic, and biological properties [8]. The properties of metal oxide nanoparticles are heavily dependent on the size, crystallinity, surface defects, and interaction of nanoparticles surface with the surrounding chemical environment [9]. Out of all the listed nanoparticles, cerium oxide nanoparticle was special interest due to the stability of cerium oxide, its high oxygen storage capacity, and reversible redox transition between Ce^{3+} and Ce^{4+} valance states [10-13]. Oxygen vacancy formation and the modification of the electronic structure of the surface result in the catalytic properties of CeO_2 nanoparticles. Because of their photocatalytic and pollutant degradation properties and antimicrobial activity, CeO_2 nanoparticles are very important materials for research [14-16]. The functional properties of cerium oxide nanoparticles depend on the preparation method and physicochemical properties of nanoparticles [17].

The conventional synthesis methods for preparing CeO_2 nanoparticles are chemical precipitation, sol-gel method, hydrothermal process, and thermal decomposition [18]. While such conventional methods offer a way of controlling nanoparticle size and crystallinity, some involve hazardous chemicals, high temperature, considerable energy consumption, or even additional purification steps [19]. In order to find a safer synthesis method, green synthesis became an alternative method involving the use of biological components for nanoparticle formation [20]. The synthesis using plant extracts is especially interesting since the plant components contain natural phytochemicals that can affect the interaction with metal precursors during the nanoparticle formation [21-25]. Phytochemicals such as phenolics, flavonoids, tannins, terpenoids, and organic acid can take part in complexation with the precursor and be incorporated into nanoparticles surface [26-27]. However, the role of the phytochemicals depends on extract composition and synthesis conditions [28-29].

Bark of plants constitutes a significant biological source for green synthesis of nanoparticles owing to the presence of various secondary metabolites in the form of chemicals used by the plants for defence and interaction [30]. In comparison with plant leaves which are more commonly studies of phytochemicals for development of functional nanomaterials, the bark of plants provides an alternative option [31]. *Anogeissus latifolia* belongs to the Combretaceae family native to India and Southeast Asia and is a medicinal plant known for its usage as well as the phytochemical composition [30]. Previous research work has shown the presence of phenols and antimicrobial properties in the extract of this particular plant [32]. The bark of the *Eucalyptus camaldulensis, Calotropis procera* flower *and Melastoma sp.* leaf were used as a biological source for the biosynthesis of CeO_2 nanoparticles owing to the naturally available tannins and other phenols that can affect the growth and aggregation of particles [33-35]. However, the exact involvement of these phytochemicals in the process of synthesis can only be confirmed through experiments rather than being deduced based on the existing knowledge about the phytochemical composition of the plant [36-38].

Earlier studies have shown the possibility of applying plant mediated CeO_2 nanoparticles in the field of photocatalysis and biocatalysis [39]. Studies on the review of green synthesized cerium oxide nanoparticles showed their potential for dye degradation, pollutants removal, and antimicrobial studies [40]. This means that the plant-based synthesis processes can affect the structure of nanoparticles and allow multifunctional application [41]. However, results achieved by using different plants cannot be generalized to *A. latifolia* bark since they might differ from one another due to difference phytochemistry and process conditions [42]. Therefore, to prove the novelty of this study, it is needed to consider if this particular bark was ever applied to biosynthesize CeO_2 nanoparticles and investigate their photocatalytic and antimicrobial properties [43].

Degradation by photocatalysis is one of the techniques that have been used for the removal of wastewater with persistent organic dye pollutants [44]. Rhodamine B (RhB), which is an artificial xanthene dye, has been utilized as a pollutant model when it comes to assessing the efficacy of photocatalytic materials [45]. When exposed to adequate radiation, CeO_2 nanoparticles can promote surface reaction using photogenerated charge carries and reactive oxygen species and consequently bring about changes in dye molecules [46]. The activity of such nanoparticles in terms of photocatalysis depends on various factors such as catalyst concentration, initial concentration of dye, solution pH, radiation exposure, and reaction time [47]. Proper dark adsorption and photolysis controls must be performed to differentiate between photocatalytic degradation, adsorption, and photochemical degradation [48].

In addition to environment use, CeO_2 nanoparticles could also be effectively tested for their efficacy as antibacterial and antifungal [49]. The effects of such nanomaterials on microbes include alternation of membrane integrity, oxidative stress, and others, but their exact mechanism of action is dictated by the physicochemical properties of the nanoparticles and the testing conditions [50]. Antibacterial activities could be examined in Gram-positive *Staphylococcus aureus* and Gram- negative *Escherichia coli* bacteria, while the MIC test measures the concentration that inhibits visible growth [51-52]. Similar antifungal activities could be determined in *Aspergillus niger and Candida albicans* fungi [53-54]. Microbial controls and antimicrobial references should always be included.

Consequently, in the present study, cerium oxide nanoparticles (D-CeO_2) were successfully biosynthesized using medicinal *Anogeissus latifolia* bark extract through a green synthesis approach. The synthesized nanoparticles were characterized to investigate their structural, morphological, and physicochemical properties. Their photocatalytic activity was evaluated through the degradation of Rhodamine B dye under controlled irradiation conditions, while their biological activities were assessed through antifungal assays and antibacterial minimum inhibitory concentration (MIC) tests. This comprehensive investigation explored the functional properties of D-CeO_2 nanoparticles synthesized using *A. latifolia* bark extract and evaluated their potential applications in environmental remediation and antimicrobial fields.

2. Material and Methods

2.1 Materials

Cerium nitrate hexahydrate [$Ce(NO_3)_3 \cdot 6H_2O$], ethanol (C_2H_5OH), sodium hydroxide (NaOH), and Rhodamine B dye were used as received from manufacturers. Bark of *Anogeissus latifolia* (Dhawada) plant was collected from the Karandla forest, Umrer, Nagpur, Maharashtra, India.

2.2 Plant Material Used

Anogeissus latifolia is referred to as Dhaura, Dhau, Vekkali, or Dhawa and is popularly called as Dhawada, Gahtti, Axlewood or Dhawra, is native to Indian and South-East Asia. This deciduous tree belonging to the Combretaceae family, is of medicinal, ecological, and economic importance [55-56]. Several parts of *Anogeissus latifolia* like the bark, leaves, and gum, have been used traditionally in medicine systems like Ayurvedic and Siddha medicine, in treatment of wounds, diarrhea, diabetes, fever, cuts, ulcers and many other conditions. The use of this plant in the treatment of diseases like syphilis, gonorrhea, scorpion, and snake bites is

indicative of its ethnobotanical importance. The bark of the tree is grayish-white and smooth. The phytochemical studies have shown the presence of bioactive compounds like tannins, flavonoids, phenolics, terpenoids, steroids, saponins, alkaloids, carbohydrate, quinones, anthraquinone, and glycosides. These chemical compounds contribute for many pharmacological activities, such as antioxidants, antimicrobials, anti-inflammatory agents, antidiabetic, hepatoprotectants, anti-ulcer, and wound-healing activities [57-59].

2.3 Bark Extract Preparation

The collected bark of *Anogeissus latifolia* was first washed with tap water to remove surface soil particles, then rinsed several times with distilled water. Subsequently, the clean bark was air-dried under natural sunlight and ground into a fine powder using a mechanical mixer. The resulting dried powder was stored in a dry environment until further use. For extract preparation, 10 g of the bark powder was dissolved in a mixture of 100 mL deionized water and 50 mL ethanol and the mixture was boiled for 2 h at 70 °C until it turned into a brown extract. The extraction was allowed to cool to room temperature, and bark extracts were obtained after centrifugation of the aqueous solution at 5000 rpm for 20 minutes, filtered through Whatman filter paper no. 1, and stored at 4 °C for further experimentation. A schematic representation of the extraction process as shown in Fig. 1.

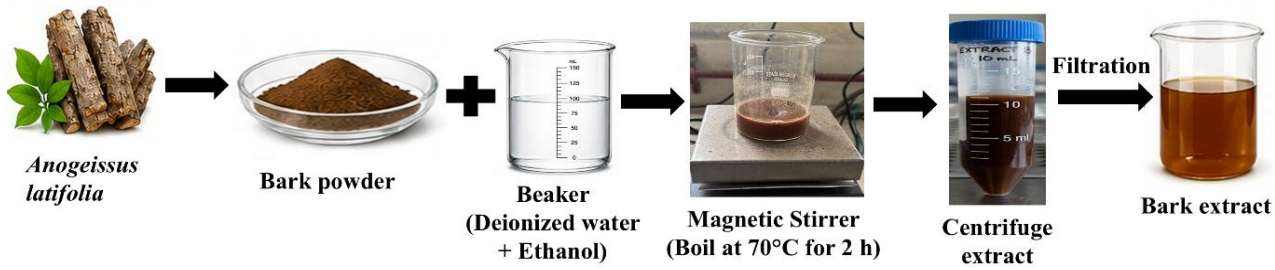


Fig. 1. Illustration of preparation of bark extract.

2.4 Phytochemical Screening of the Plant Extracts

The qualitative phytochemical screening of the aqueous bark extract of *Anogeissus latifolia* for constituent like tannins, flavonoids, phenolics, triterpenoids, steroids, saponins, alkaloids, and glycosides were tested according to the literature [60].

2.5 Biosynthesis of D-CeO_2 NPs

The D-CeO_2-NPs were biosynthesized using the following method, with slight modifications: The precursor for biosynthesizing CeO_2 NPs, 0.1 M $Ce(NO_3)_3.6H_2O$ were diluted in 40 mL of deionized water with constant stirring at room temperature for 20 min.

Phytochemicals present in a *Anogeissus latifolia* bark extract was used as reducing agents. 20 mL of the prepared bark extract dropwise added to the homogeneous solution of 0.1 M $Ce(NO_3)_3.6H_2O$ salt, and then the mixture was stirred for 2 h at 70 °C and 1000 rpm. The pH of mixture was regulated using 2 M sodium hydroxide (NaOH) and adjusted to pH 11. The color of solution changed from colorless to pale yellow and finally to extremely sticky and dark brown-colored gel was obtained. The sticky gel solution was centrifuged at 10000 rpm for 10 minutes, and filtered to separate the product. The product obtained was dried in an oven at 100 °C for 6 h. Finally, the dark brown-dried powdered product was calcinated in a muffle furnace at 500 °C for 4 h to obtain a yellowish-white precipitate in its purest form. The obtained yellowish-white precipitate was purified by washing it thoroughly with deionized water and ethanol to obtain purified D-CeO_2 NPs were created, and the chemical equation (1) and (2) below reflect this. Additionally, a systematic diagram was given to explain the synthesis process shown in Fig. 2.

$$Ce(NO_3)_3.6H_2O_{(S)} + \text{Phytochemicals (green source)}_{(l)} \rightarrow Ce(OH)_{3(S)} \quad \text{.....(1)}$$

$$4Ce(OH)_{3(S)} + O_2 \rightarrow 4CeO_{2(S)} + 6H_2O_{(l)} \quad \text{.....(2)}$$

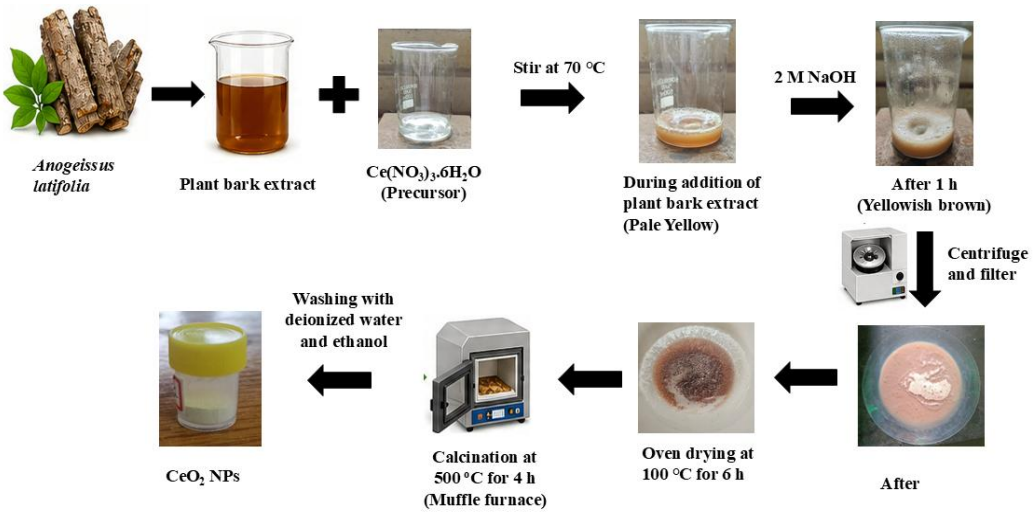


Fig. 2. Schematic representation of biosynthesis of D-CeO_2-NPs.

2.6 Measurements

The biosynthesized D-CeO_2 NPs was characterized in several spectroscopic and analytical techniques, X-ray diffraction (XRD) was performed by Rigaku (Miniflex 600) diffractometer for the 2θ value ranging from 20° to 80° using Cu Kα radiation at λ =0.154 nm. UV-visible diffuse reflectance spectra were recorded by using UV-Vis-NIR (JASCO V-670) spectrophotometer. Fourier transform-infrared (FT-IR) (Shimadzu, IRAffinity-1, Thermo

Nicolet iS50) with KBr pellets technique was used to record spectra in the range 400–4000 cm^{-1}. Thermogravimetric analysis (TG) (TA Instruments, USA, SDT Q600) was evaluate thermal stability and degradation behavior. Fluorescence spectrometer (PL) (Hitachi F-7000) used for measuring fluorescence spectra in UV- Visible region (220-700 nm), The surface morphology was analysed by scanning electron microscopy (SEM) carried out using JEOL 6390LA/OXFORD XMX N and high resolution transmission electron microscopy (HRTEM) by using JEOL/JEM 2100, Energy Dispersive X-ray spectroscopy (EDX) analysis carried out by using JEOL 6390LA/OXFORD XMX N at accelerating voltages of 0.5 to 30 kV, and pH ION/EC/DO METER (MM-43X) was used to measure the pH of the solution.

2.7 Photocatalytic Activity of D-CeO_2 NPs

The photocatalytic activity of D-CeO_2 NPs was assessed based on rhodamine B (RhB) being used as a dye. For this purpose, a typical test was performed where stock solution of rhodamine B of concentration 10^{-3} M was prepared. 3 mL of RhB was taken from the stock solution and diluted RhB solution. Then, a fixed quantity of (30 mg) photo-catalyst was added to 100 mL (10^{-3}) of RhB dye. The photocatalysis was started at an interval of 30 minutes in the presence of UV radiation. Absorbance of all the solution was measured using a UV-Visible spectrophotometer at 586.4 nm. The efficiency of the process was calculated from the following equation (3).

$$\text{Photocatalytic degradation (\%)} = \frac{C_0 - C_t}{C_0} \times 100 \qquad \text{……..(3)}$$

Where, C_0 = Initial concentration and C_t = Concentration after various time intervals (min)

2.8 Antibacterial Activity of D-CeO_2 NPs

In this study, the antibacterial activity of the D-CeO_2 NPs was investigated. The two bacterial strains, such as *S. aureus* and *E. coli* were acquired from the Hi-Media Pvt. Ltd. in Mumbai, India.

Microdilution broth method was applied for MIC determination of the compounds following to Clinical and Laboratory Standards Institute (CLSI) criteria. In this context, two-fold serial dilutions of compounds were made in 100 µL of the suspension of the tested bacteria with final concentration of 5 $\times 10^5$ CFU/mL was added to each well of the plate. Bacterial suspension in Mueller Hinton Broth medium and the medium itself were considered as positive and negative control, respectively. the plates were incubated for 18-24 h at 37 °C. The minimal concentration of the compound that prevented bacterial growth (no turbidity) was considered as MIC value.

2.9 Antifungal Activity of D-CeO_2 NPs

The antifungal activity of biosynthesized D-CeO_2 NPs was tested against *A. niger* (strain AS14) and *C. albicans* (strain CA10) using the agar well diffusion method. Fresh cultures of Strain-AS14 and strain-CA10 were grown in potato dextrose broth medium for 24 h and inoculated by lawn culture technique on sterile solidified Potato Dextrose Agar (Himedia-MH096) plates with the help of sterile cotton swabs. The stock solutions with a concentration of 1 mg/mL were prepared in DMSO solvents. Three wells were bored on the PDA media plates with the help of a sterile cork borer (8 mm) and loaded with D-CeO_2-NPs solutions following concentrations: 25 µL (25 µg), 50 µL (50 µg), and 100 µL (100 µg), respectively. Then allow it to diffuse at room temperature for 2 to 3 h. The plates were incubated in an upright position at 30 °C for 72 h. Then the zone of inhibition was observed. In control plates, 100 µL of DMSO was added as a negative control and an antibiotic disc as a positive control. For Strain- AS14 and strain CA10 Itraconazole 30 mcg was used.

3. Results and Discussion

3.1 Phytochemical Screening of the Plant Bark Extracts

The results obtained from the analysis of the phytochemical screening of the *Anogeissus latifolia* bark extract show the presence of alkaloids, glycosides, quinones, saponins, flavonoids, phenols, carbohydrates, steroids, tannins, terpenoids, and anthraquinone as shown in Fig. 3. The flavonoids and tannins were strongly present, but that of glycosides, terpenoids, and anthraquinone was least present. The outcomes of the qualitative phytochemical screening analysis of bark extract were shown in Table 1. This means that the presence of such secondary metabolites has facilitated the reduction and stabilization role of the *Anogeissus latifolia* bark extract during the preparation of D-CeO_2 NPs. The findings have been made; the discovery is in agreement with previous works on the phytochemical screening [60].

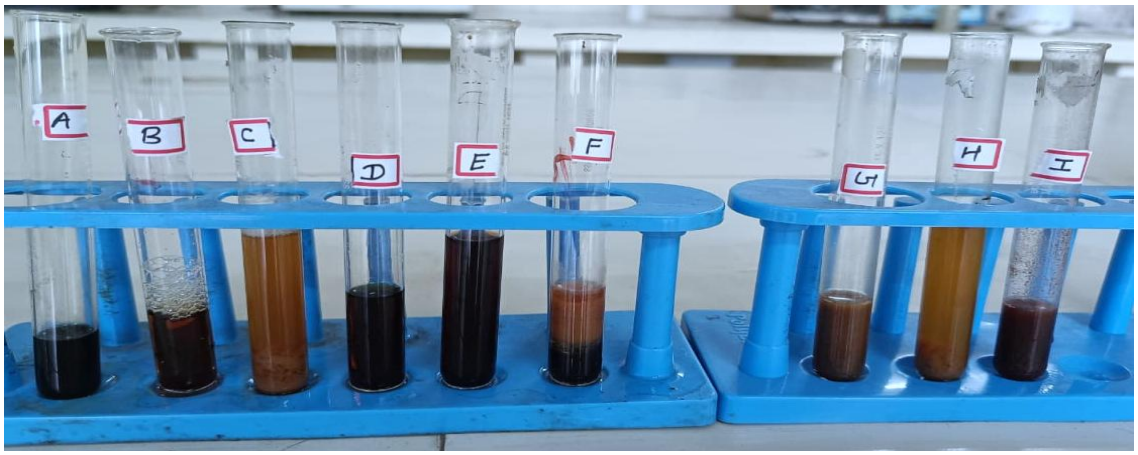


Fig. 3. The observation of different test of phytochemical.

Code	Phytochemicals	Tests	Observation	Result
A	Tannins	Distilled water and ferric chloride	black precipitate was observed	+++
B	Saponins	Distilled water and aggressively shaken to produce foam froth and olive oil	Examined for emulsion development.	++
C	Flavonoids	Dilute ammonium solution and concentrated sulphuric acid	yellow or pink-red coloration was observed	+++
D	Glycosides	Ferric chloride and concentrated sulphuric acid were added into 5 mL bark extract in glacial acetic acid.	A reddish-brown coloration at the junction of two layers and a blueish green color in the upper layer was observed	+
E	Anthraquinone	10 % ammonia solution	Pink precipitate was observed	+
F	Terpenoids	Chloroform and concentrated sulfuric acid	Reddish-brown color was observed	+++
G	Sterols	Concentrated sulfuric acid	Red colouration was observed	++
H	Alkaloids	2 % hydrochloric acid and Mayer's reagent	Turbidity or red precipitate was observed	++
I	Carbohydrate	Molisch's reagent and concentrated sulfuric acid	purple or reddish color was observed	++
(+) Least present, (++) Moderately present, (+++) Strongly present				

Table 1. Result of phytochemical screening of *Anogeissus latifolia* bark extract.

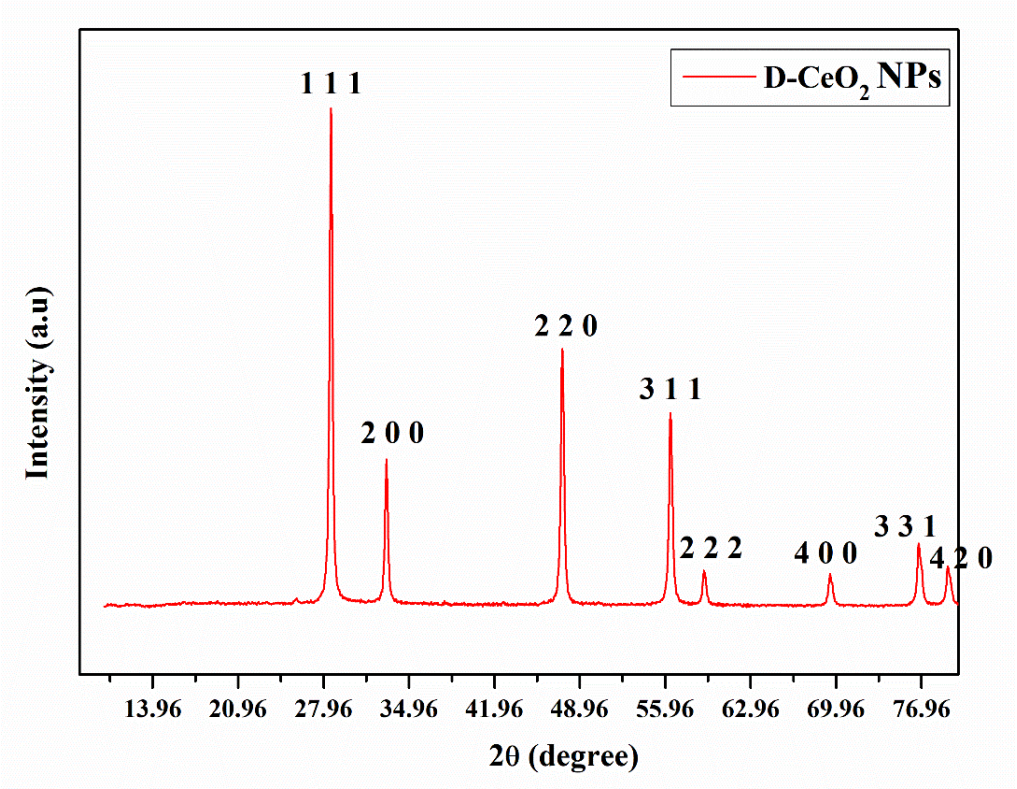
3.2 Characterization of D-CeO_2 NPs

3.2.1 X-ray Diffraction analysis

This analytic approach was utilized to ascertain the distinct crystalline phases of binary metal oxide nanoparticles as shown in Fig. 4. displays the XRD pattern of biosynthesized D-CeO_2 NPs from *Anogeissus latifolia* bark extract. The D-CeO_2 NPs confirmed the Face centred cubic fluorite crystal structure, and the XRD pattern revealed the presence of cerium oxide phases. The D-CeO_2 NPs Exhibits the peaks at 2Ɵ values at 28.55°, 33.08°, 47.47°, 56.33°, 59.08°, 69.4°, 76.69°, 79.07° and corresponding to hkl planes (1 1 1), (2 0 0), (2 2 0), (3 1 1), (2 2 2), (4 0 0), (3 3 1), (4 2 0) respectively, supported by JCPDS no. 34-0394. The lattice

parameter, including unit volume, crystalline size, micro strain, and dislocation density of D-CeO_2 NPs represented in Table 2 [61].

The lattice parameter "*a*" was estimated as 5.411 Å (0.5411 nm) by using equation (4) for biosynthesized NPs. It possessed an exceptional degree of crystallinity and a single-phase cubic fluorite crystal structure inside the ($Fm\bar{3}m$) space group. Beside the unit volume of produced green NPs was found to be 158.428 $Å^3$ (0.158428 nm^3), calculated by using the following equation (5)[62]. The average crystallite size of D-CeO_2 was calculated using the Debye-Scherrer formula shown in equation (6) [63]. Where D = crystallite size, λ = X-ray wavelength of CuKα radiation, β = Full width half maximum of the peak, and Θ represents Bragg's diffraction angle. The average crystallite size of biosynthesized D-CeO_2 NPs was calculated at 36.73 nm. Another important parameter, such as the micro-strain of D-CeO_2 NPs, was calculated using equation (7)[61]. It was noted that the calculated micro-strain of D-CeO_2 was 0.944×10^{-3}, and a crystallographic defect infers to an imperfection in the crystal structure. The dislocation density of D-CeO_2 NPs was mathematically calculated using the equation (8) [61]. Where 0.741×10^{-3} = Dislocation density of the biosynthesized D-CeO_2 NPs, which shows the electrochemical and catalytic characteristics. In addition, many researchers reported that different sources were used for the biosynthesized of CeO_2 NPs. Those parameter values of XRD were relatable with this work and comparison showed in Table 3 [64-65].



269 **Fig. 4.** XRD spectra of D-CeO_2 NPs.

Sample Name	Parameters	Equation	Equation Number	References
D-CeO_2	Lattice parameter, a (nm)	$a = \frac{\lambda}{2\sin\theta}\sqrt{h^2+k^2+l^2}$	4	[61]
	Unit Volume (a^3) nm^3	$V = a^3$	5	[62]
	average crystallite size (D) nm	$(D) = \frac{0.9\,\lambda}{\beta\cos\theta}$	6	[63]
	Micro strain (ε) × 10^{-3}	$\varepsilon = \frac{cos\theta}{4}$	7	[61]
	Dislocation density (δ) × 10^{-3}	$\delta = \frac{1}{D^2}$	8	[61]

270 **Table 2.** Different parameters of D-CeO_2 NPs from XRD.

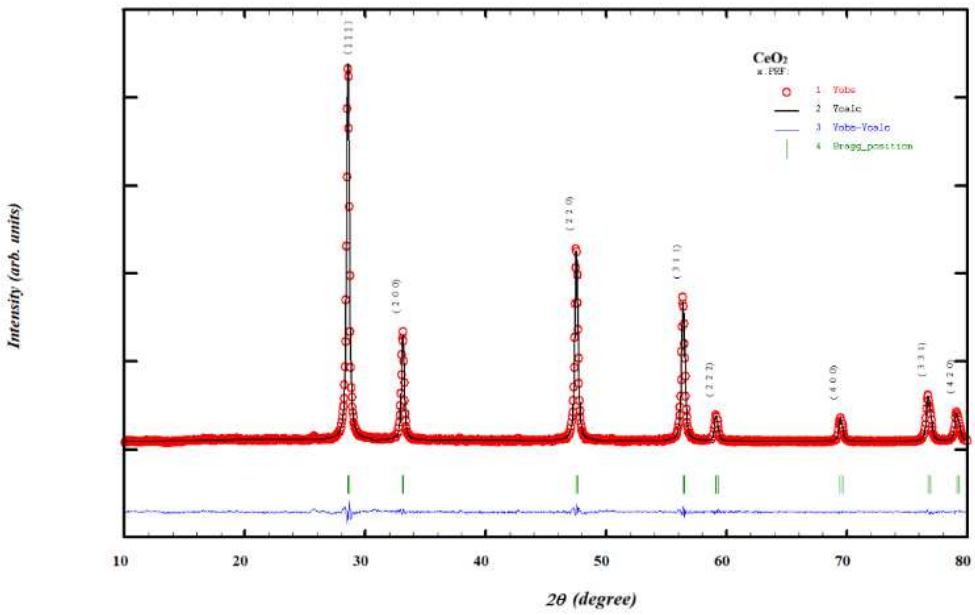
Different Source of Biosynthesized CeO_2 NPs	Lattice Parameter, a (nm)	Unit Volume (a^3) nm^3	Average Crystallite size (D) nm	Micro strain (ε) × 10^{-3}	Dislocation density (δ) × 10^{-3}	References
Abelmoschus esculentus fruit extract	0.5435	0.16054	30	1.284	1.111	[63]
Gloriosa superba L. leaf extract	0.5416	0.158867	24	1.605	1.73	[62]
Portulaca oleracea leaves extract	0.542	0.15922	16	2.407	3.906	[64]
Ficus carica fruit extract	0.541	0.15834	11.30	3.408	7.831	[65]
Oroxylum indicum fruit extract	0.5405	0.157901	23.58	1.48	1.79	[26]

Anogeissus latifolia bark extract	0.5411	0.158428	36.73	0.944	0.741	This work

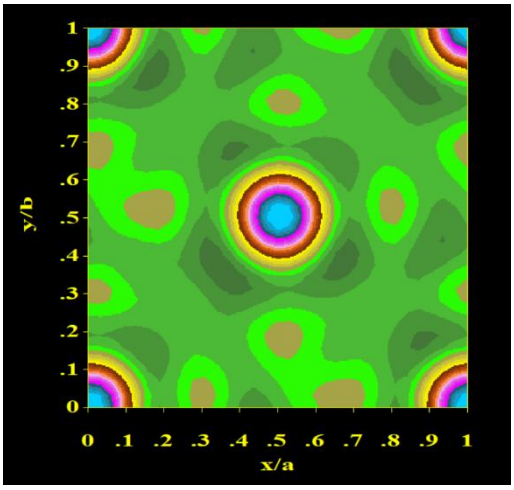
Table 3. Comparison of the XRD parameters of D-CeO_2 NPs biosynthesized from *Anogeissus latifolia* with those from different sources.

3.2.2 Rietveld Refinement

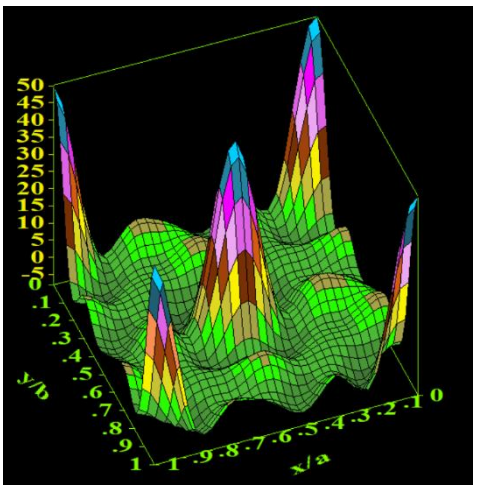
The biosynthesized D-CeO_2 NPs were refined using the Rietveld method with the aid of the Full-Prof Suite application and Vista Software. Fig 5(a) shows the refinement plot of D-CeO_2 NPs. Straightforwardly, the findings of an X-ray structural determined are electron density maps. Essentially, electron density maps are the results of an X-ray structural determination. The electron density mapping, which shows the locations of electrons, oxygen, and cerium, was explained in Fig.5(b) and (c). The maps show how well the structural model fits the data that was collected through empirical means. By using Vista software and XRD data, the crystal structure was created, as shown in Fig. 5(d)-(f). The crystal structure of cerium oxide was now visible in Fig.5(d). To illustrate the locations of the atomic layers, showed a single layer of cerium oxide in Fig.5(e)[66]. Fig.5(f) was the final representation of the polyhedral structure of cerium oxide. In addition to having 78 atoms, 112 bonds, and 14 polyhedral units, figures show the unit cell structures of D-CeO_2.The structural parameters obtained from Rietveld refinement analysis alongside the standard reference CIF data were summarized in Table 4.



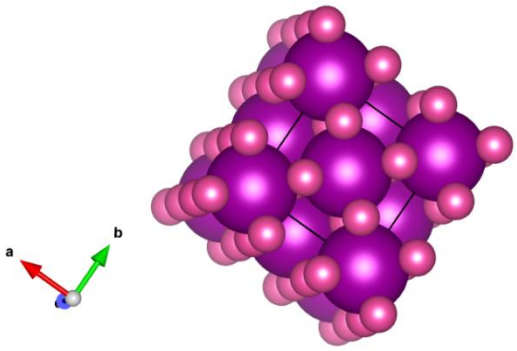
(a)

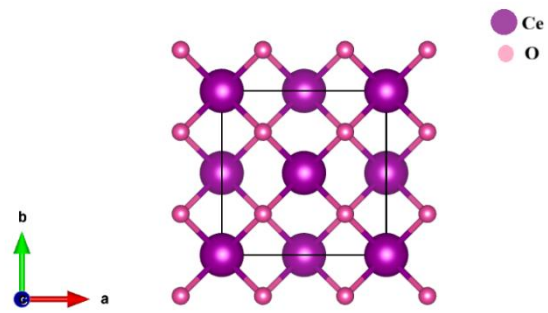


(b)



(c)

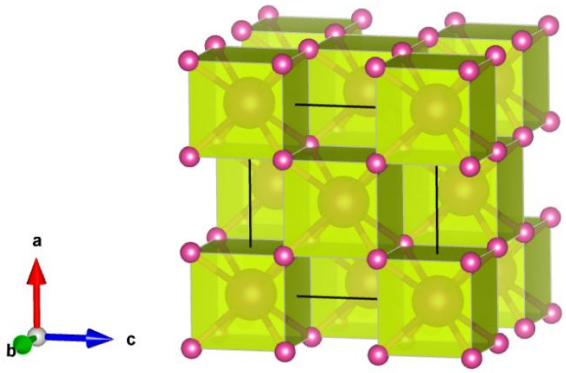




308

(d)

(e)



(f)

Fig. 5. (a) Rietveld refinement graph; (b) electron density mapping in 2D counter form; (c) electron density mapping in 3D form; (d) crystal structure of D-CeO_2 NPs in the single unit cell; (e) crystal structure of D-CeO_2 NPs in a single layer; and (f) crystal structure in a polyhedral structure.

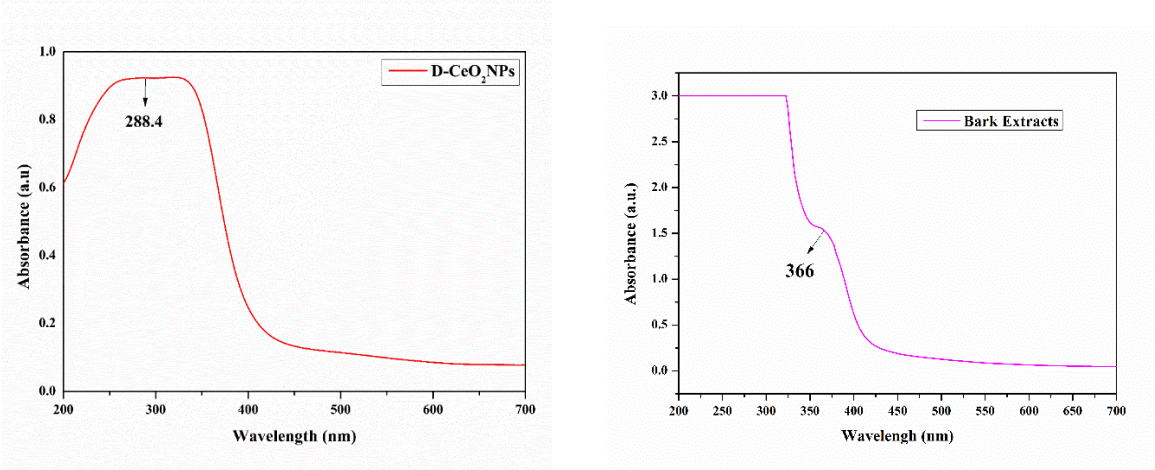
Sr No.	Parameters	Rietveld Refinement	Standard CIF reference
1	Crystal Structure	single-phase cubic fluorite	single-phase cubic fluorite
2	Space group	$Fm\bar{3}m$	$Fm\bar{3}m$
3	Number of Space group	227	—
4	Point group	m-3m	—
5	Bravais Lattice	F	—
6	a	5.40998 Å	5.411 Å
7	b	5.40998 Å	5.411 Å
8	c	5.40998 Å	5.411 Å
9	Unit-cell volume	158.338649 $Å^3$	158.428 $Å^3$
10	α	90°	90°
11	β	90°	90°
12	γ	90°	90°
13	Rp	11.5	—
14	Rwp	10.4	—
15	Chi (c^2)	1.09	—
16	RF-Factor	4.43	—
17	DW-Stat	0.8813	—
18	Goodness of fit	0.792	—

Table 4. Crystallographic parameters and Rietveld refinement data comparison with standard CIF reference.

3.2.3 Ultraviolet-Visible-NIR Spectroscopy

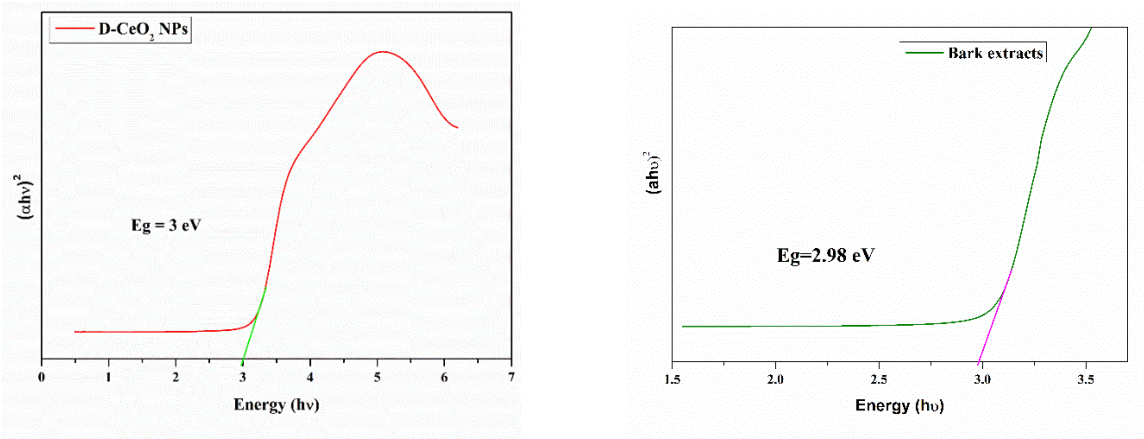
The UV-Vis-NIR adsorption spectrum was obtained for the study of optical properties of D-CeO_2 NPs biosynthesized using *Anogeissus latifolia,* plotted as absorbance (a.u.) versus wavenumber (nm). The biosynthesized material showed a strong absorption peak at 288.4 nm, indicating the formation of D-CeO_2 NPs. as shown in Fig. 6(a). While Fig.6(b) showed the absorption peak at 366 nm, which indicates the presence of the bark extract in biomolecules.

The optical band gap value was calculated using the Tauc plot method by plotting $(\alpha h\upsilon)^2$ versus energy ($h\upsilon$), where α stands for the absorption coefficient and $h\upsilon$ is the photon energy (eV), as shown in Fig. 7(a) and (b). The direct band gap energy for D-CeO_2 NPs and bark extracts was calculated 3 eV and 2.98 eV respectively, from the intercept of the linear region of the plot on the energy axis.



(a) (b)

Fig. 6. UV–Vis-NIR spectra: (a) D-CeO_2 NPs, (b) Bark extracts.



(a) (b)

Fig. 7. Tauc plot spectra: (a) D-CeO_2 NPs, (b) Bark extracts.

3.2.4 FT-IR Spectroscopy

The FT-IR spectra of D-CeO_2 were examined against the wavenumber (cm^{-1}) versus transmittance (%) shown in Fig.8. To determine the composition and functional groups of biosynthesized D-CeO_2 NPs, FT-IR spectra were recorded in the range of 4000 - 450 cm^{-1}. The absorption band 3464.15 cm^{-1} can be assigned to the O-H stretching vibration of physically

adsorbed water molecules and surface hydroxyl groups. The absorption band 1581.63 cm^{-1} can be assigned to the bending vibrations of surface adsorbed moisture (H-O-H) with carbonyl (C=O) or conjugated aromatic or alkene skeletal vibrations from the organic capping or reducing agents. The absorption band at 1388.75 cm^{-1} corresponds to the symmetric stretching vibrations of nitrate ions (NO_3^-) from the cerium nitrate precursor. The band at 1060.85 cm^{-1} and 979.84 cm^{-1} represents to C-O stretching vibrations and Ce-OH bending vibrations respectively. The absorption band at 412.77 cm^{-1} and 648.08 cm^{-1} indicate the Ce-O lattice vibration mode in the cubic fluorite structure of ceria in the D-CeO_2 nanoparticles.

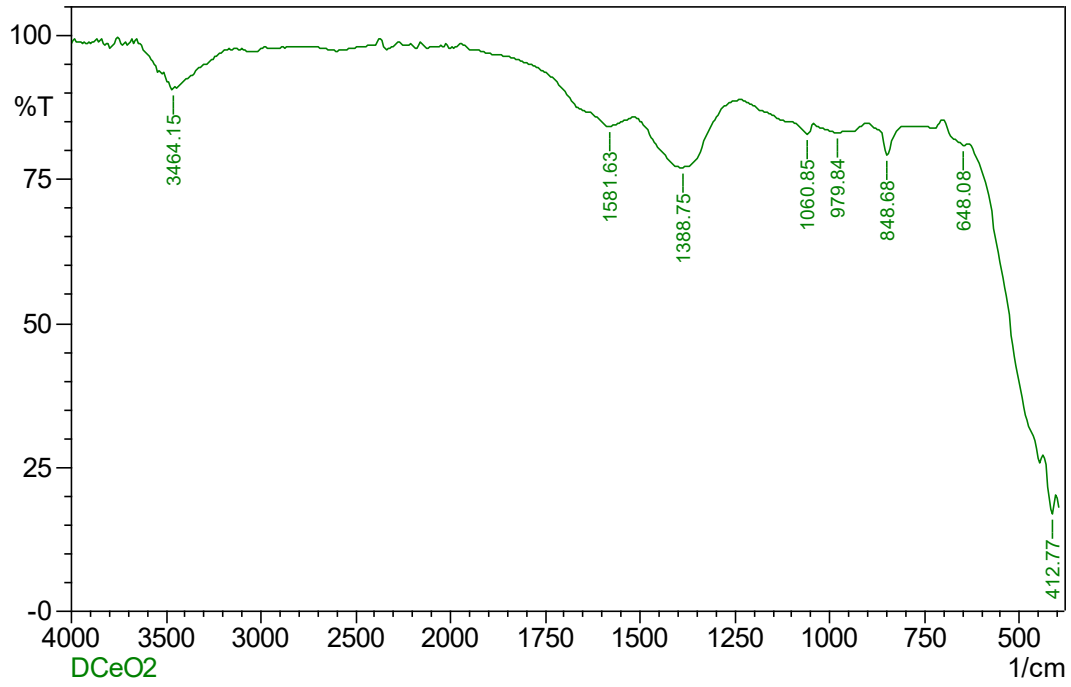


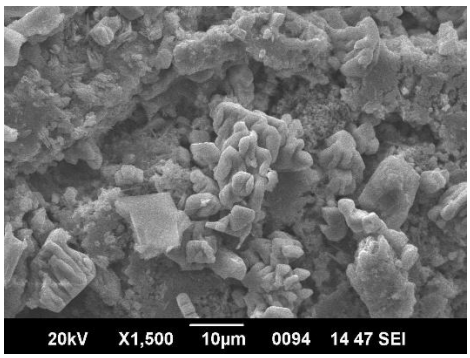
Fig. 8. FT-IR spectra of D-CeO_2 NPs.

3.2.5 Scanning Electron Microscopy with Energy-Dispersive X-ray Spectroscopy Analysis

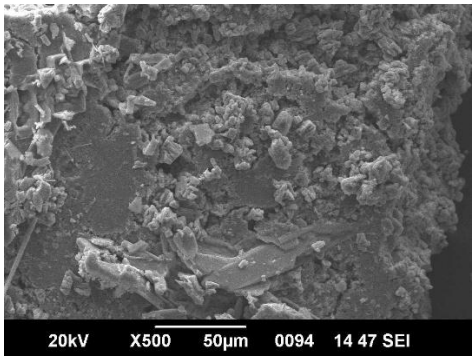
The scanning electron microscopy with energy-dispersive X-ray spectroscopy (SEM-EDX) analysis of *Anogeissus latifolia*-mediated CeO_2 NPs revealed their morphological characteristics, such as size, shape, surface properties, and crystallinity, which shown in Fig. 9. The following results revealed that D-CeO_2 NPs were present in a clustered form owing to high aggregation and nucleation phenomena. This was attributed to various factors such as van der Waals, electrostatic interactions, and solvent evaporation effects. The biosynthesized D-CeO_2 NPs were calcinated at 500 °C for 4 h. Small NPs aggregate to form particles of large size, and the process occurs during the calcination of the sample. The temperature factor in calcination affects the rate of aggregation and thus the increase in particle size and crystallinity with rise in temperature was observed. SEM image viewed that the irregular, rounded, polyhedral like

shapes structure that closely attached of D-CeO_2 NPs. Small nanocrystals were aggregated to form large nanocrystal. The process of aggregation depends on the aging time. The size of nanoparticles increases due to aggregation with the increase in aging time. Aggregation occurs when microspheres of proper orientation interact with each other to form monoclinic tenorite phase microsphere. The rough surface of the microsphere was due to the presence of a nanosphere on its surface. It is important to note that the observed size slightly vary owing to the aggregation of nanoparticles, leading to overlapping or partial obscuration of individual particles.

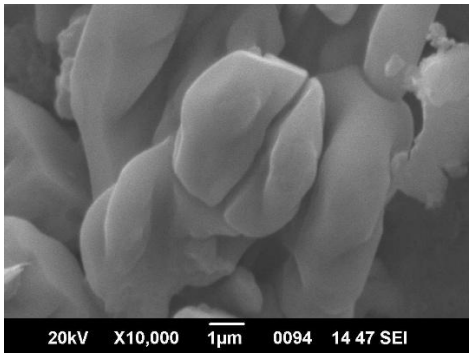
The chemical composition of the crystalline D-CeO_2 NPs was confirmed by EDX analysis as shown in Fig. 10. The EDX spectrum indicates predominant peaks for cerium elements with carbon and oxygen, suggesting exceptional purity of D-CeO_2 NPs. EDX analysis additionally verified that these D-CeO_2 nanomaterials consist of 73.2% Cerium and 20.6% Oxygen. with another peak of 6.19% carbon was detected (Table 5). This analysis provides valuable insights into the morphology and elemental composition of the biosynthesized D-CeO_2 NPs.

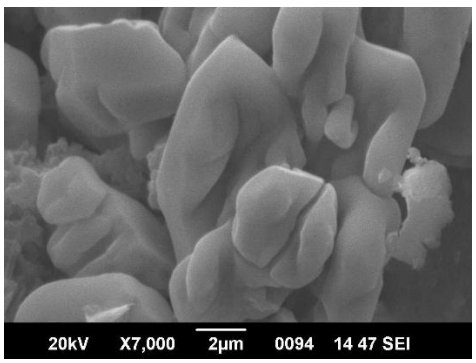


(a)

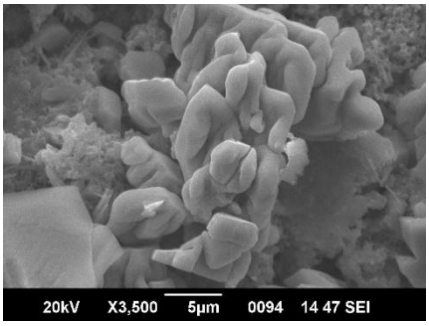


(b)





(c) (d)



(e)

Fig. 9. SEM image of (a-e) biosynthesized D-CeO_2 NPs.

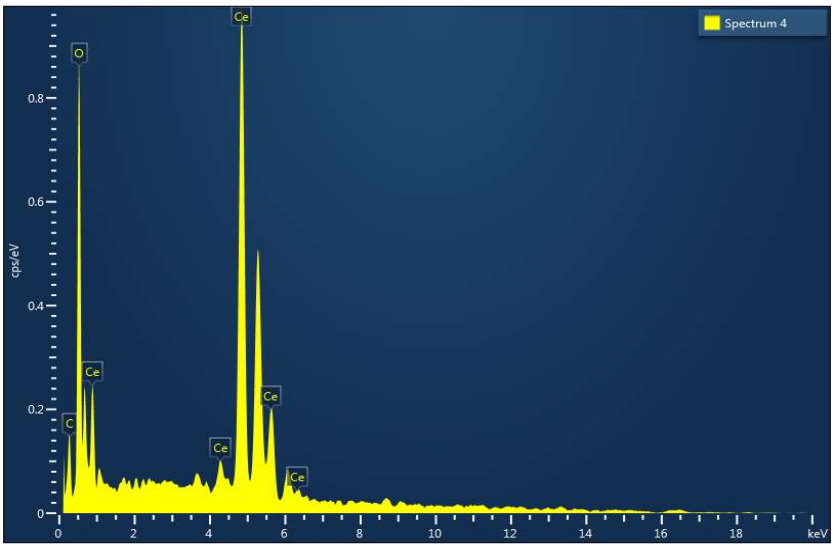


Fig. 10. EDX spectrum of biosynthesized D-CeO_2 NPs.

Element	Line Type	Weight %	Atomic %
C	K series	6.19	22.17
O	K series	20.6	55.37
Ce	L series	73.2	22.46
Total		100	100

Table 5. Elemental composition of the biosynthesized D-CeO_2 NPs.

3.2.6 Thermal Studies

The thermogravimetric analysis curve of the biosynthesized D-CeO_2 nanoparticles was presented in Fig. 11. The TG curve of D-CeO_2 NPs showed three step decomposition, and weight loss of the material was observed in the temperature range of 25-150 °C, 150-400 °C and 400-800 °C. The weight loss 0.5666 % of the material observed in the temperature range

of 25-150 °C, which was mainly due to the removal of physically adsorbed water and solvent residues. The weight loss of 1.990 % in the temperature range of 150–400 °C, which could be due to the thermal combustion of capping phytochemicals and organic functional groups responsible for steric stabilization. The condensation of hydroxyl groups and decomposition of surface carbonates at 600–790 °C. In general, from TG analysis, the total weight loss calculated was 3.46 % and 96.54 % of its mass at 800 °C, confirming the formation of the thermal stability and purity of the biosynthesized D-CeO_2 nanoparticles. The high residual mass confirms the formation of a thermally stable crystalline D-CeO_2 nanoparticles.

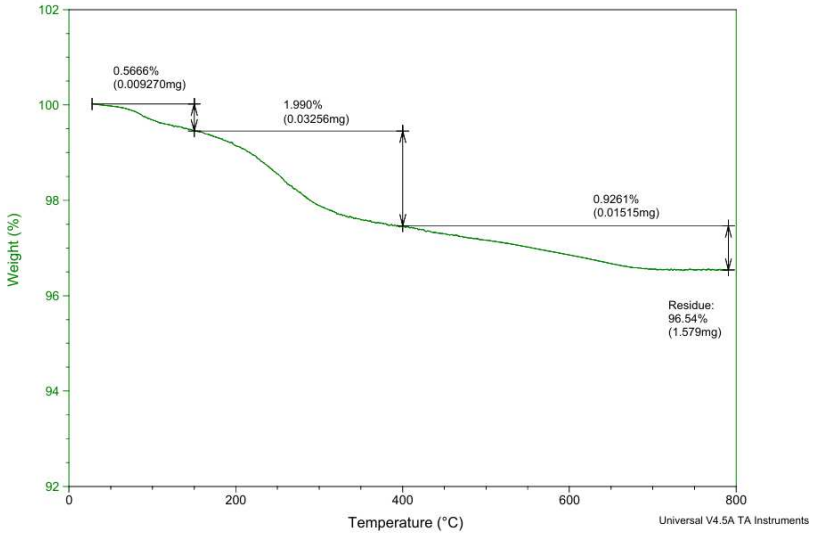
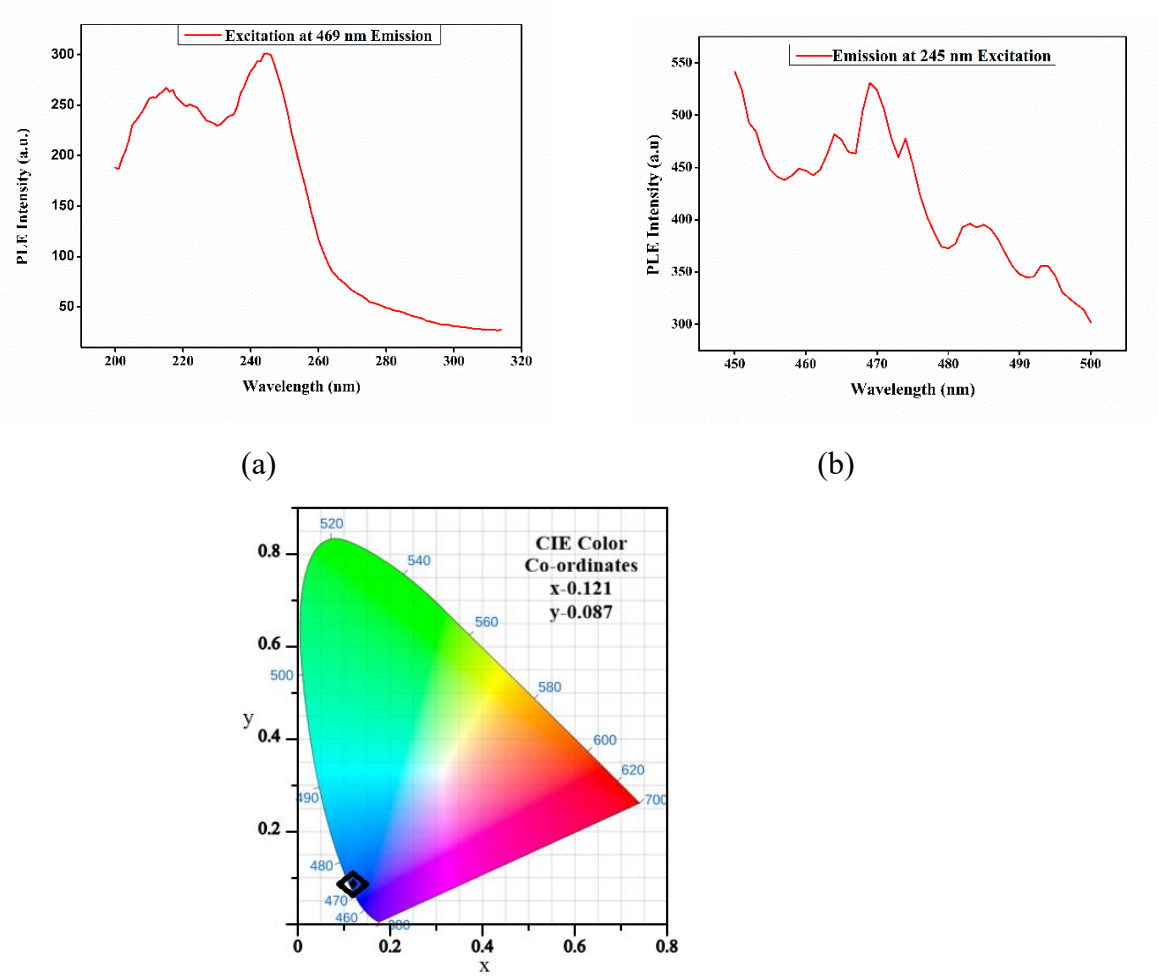


Fig. 11. TG graph of biosynthesized D-CeO_2 NPs.

3.2.7 Photoluminescence (PL) Spectroscopy

The photoluminescence excitation (PLE) spectrum measured at an emission wavelength of 469 nm. Fig.12(a) represents a distinctive excitation peak at 245 nm that was related to the fundamental charge transfer process between the occupied O^{2-} (2p) valence band and the empty Ce^{4+} (4f) orbitals. Upon excitation at the characteristic wavelength (λ_{ex} = 245 nm), the corresponding room temperature emission spectrum, Fig.12(b) showed a well-defined blue emission peak with its main peak at 469 nm and additional shoulder peaks within 450-495 nm range. As this energy of emission at 2.64 eV was lower than the optical band gap of CeO_2, the luminescence assigned to defect-assisted radiative recombination via localized electronic states, specifically, by electrons captured at oxygen vacancies (*Vo*) and by localized Ce^{3+} ions formed on the nanoparticle surface. In addition, the corresponding calculation CIE 1931 chromaticity coordinates of the emitted light were x= 0.121 and y= 0.087 as shown in Fig.12(c) and clearly situated in the deep-blue coordinates area and prove high color purity.



(a) (b)

(c)

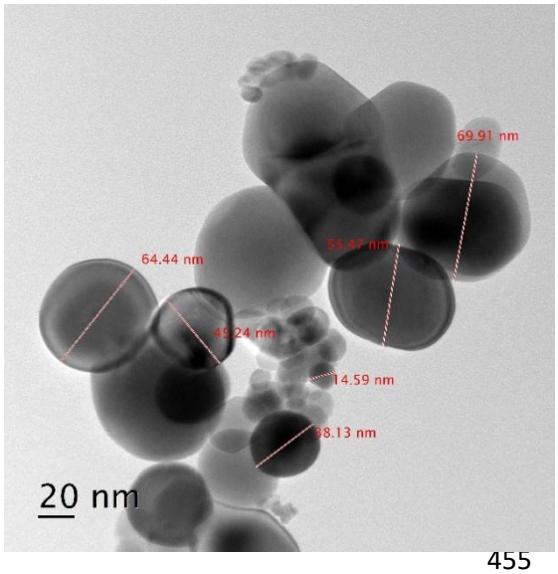
Fig. 12. Optical and photoluminescent properties of D-CeO_2: (a) PLE spectrum measured at 469 nm, (b) PL emission spectrum at 245 nm, and (c) CIE color co-ordinates.

3.2.8 Microstructural and Crystallographic Analysis

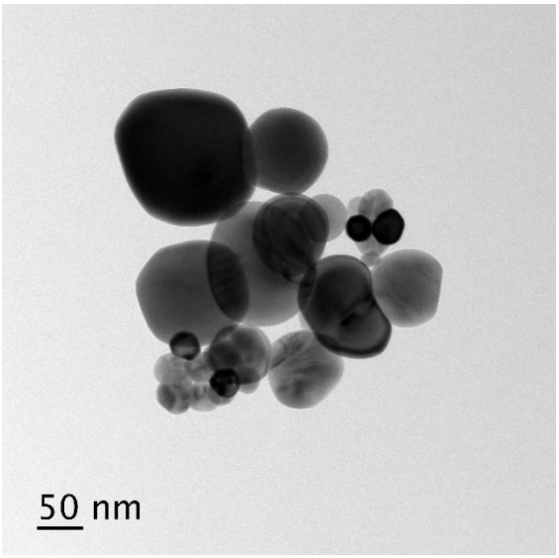
The morphological characteristics, microstructure and crystallography of the biosynthesized D-CeO_2 nanoparticles were characterized by means of high-resolution transmission electron microscopy (HRTEM) coupled with selected area electron diffraction (SAED).

It can be seen from the representative bright field HRTEM images (Fig.13. (a-b)) that the biosynthesized D-CeO_2 nanoparticles showed mostly spherical to quasispheroidal morphology with well-defined boundaries. The interparticle aggregation has been observed in many clustered areas due to high surface energy and dipole-dipole interactions at the nanoscale level. The particle size determination shows that the size varies from 14.59 nm to 69.91 nm, with the largest population of crystallites lying between 35 nm and 55 nm.

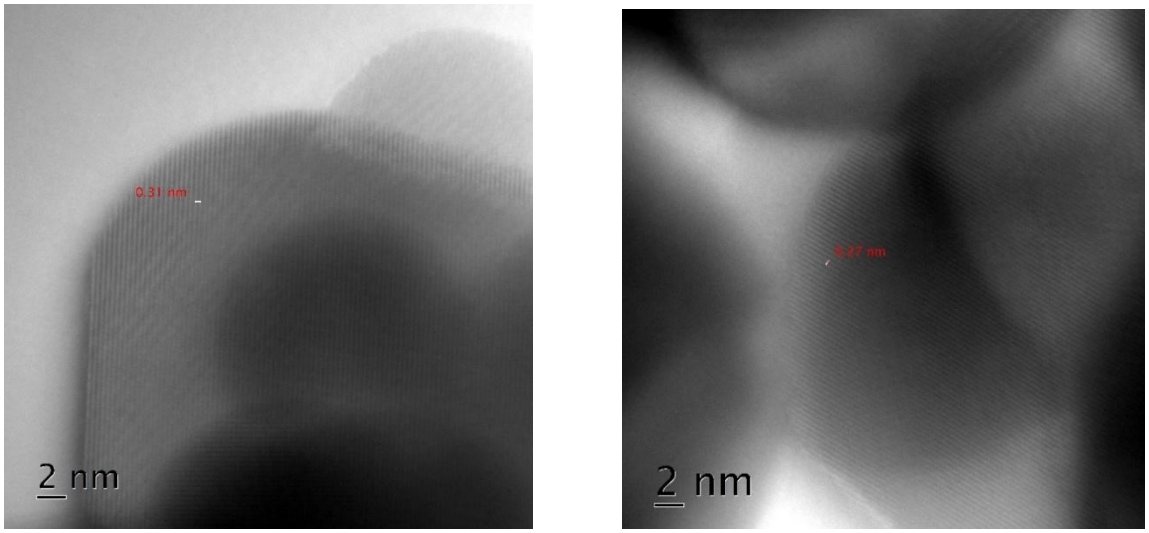
The HRTEM lattice images (Fig.13. (c-d)) unequivocally shows the presence of continues and parallel atomic fringes extending across the whole crystallite structure without the presence of an amorphous shell at the grain boundaries, indicating the excellent atomic ordering and crystallinity of the particles. The observed interplanar fringes spacing of 0.31 nm to 0.27 nm exactly matches the (1 1 1) and (2 0 0) crystal planes respectively, of cubic fluorite type CeO_2, where thermodynamically stable (1 1 1) surface dominate the crystalline growth. In addition, the SAED image (Fig.13. (e-f)) shows distinct and sharp concentric Debye-Scherrer ring made up of bright diffraction spots, which are indicative of polycrystallinity. The observed diffraction rings index unambiguously to the (1 1 1), (2 0 0), (2 2 0), (3 1 1), (2 2 2), and higher order miller planes of the face-cantered cubic (FCC) fluorite D-CeO_2 phase, corroborating the XRD phase identification without any detectable secondary phase or impurities.



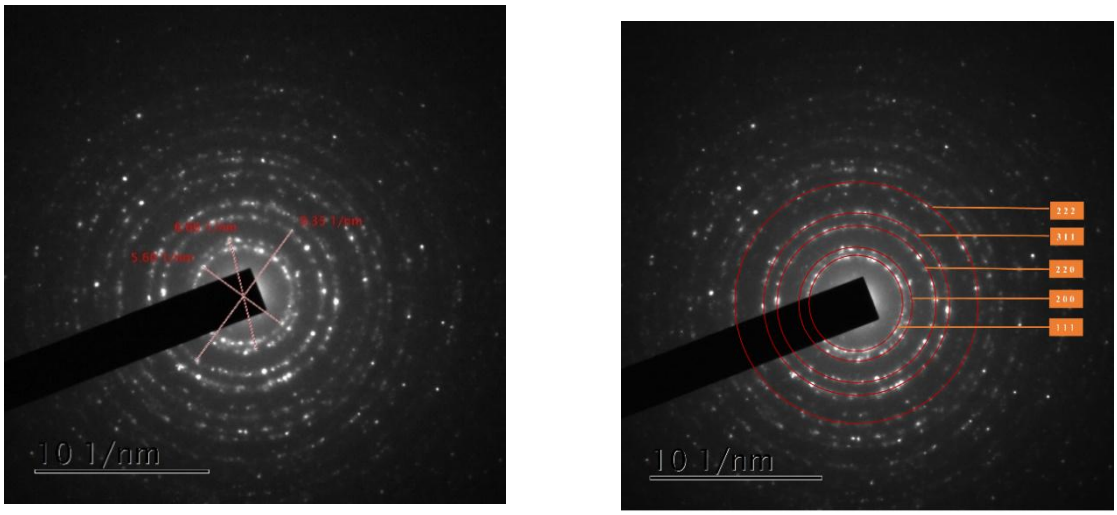
(a)



(b)



(c) (d)



(e) (f)

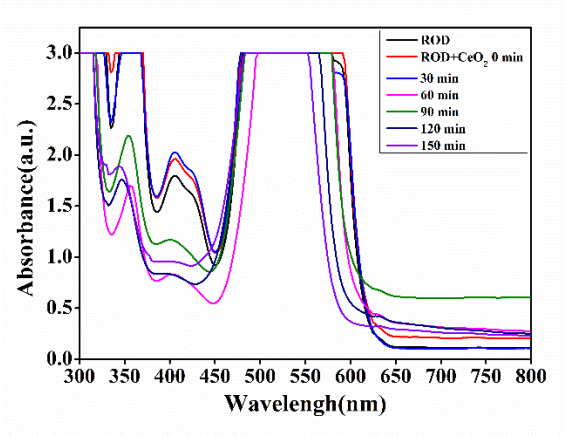
Fig. 13. HRTEM and SAED image (a-f) of D-CeO_2 NPs.

3.2.9 Photocatalytic Activity

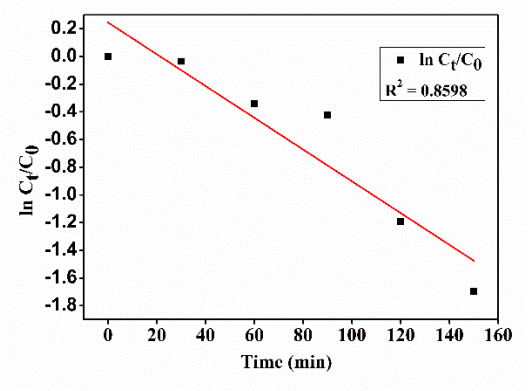
Rhodamine B (RhB) represents a major cationic xanthene dye widely employed in various industrial fields, including textiles, leather production, printing, paper and pharmaceutical. Additionally, RhB is frequently used in analytical chemistry as a fluorescent tracer and diagnostic strain. redox indicator. The complexity and stability of the aromatic structure of RhB make it resistant to natural degradation by chemicals and living organisms, making it persistent in the environment. The contamination of water bodies by RhB-containing effluents limits penetration of sunlight, thus preventing photosynthesis. Additionally, exposure to RhB results in toxic effects to living beings including cytotoxicity, neurotoxicity, skin and

eye irritation, and potentially carcinogenic effects. Therefore, the development of sustainable and efficient approaches for the photodegradation and mineralization of RhB in effluents in an important environmental challenge. In this work, the photocatalytic activity of the biosynthesized D-CeO_2 NPs was calculated using the photodegradation of RhB dye with UV light irradiation over a period of 150 min, as shown Fig.14(a). the time dependent UV- Vis absorption spectra showed characteristic absorption bands in the visible range 586.4 nm, as confirmed by efficient chromophore degradation (Fig.14(a)). this resulted in a gradual increase in degradation efficiency from 4% at 30 min to 29%, 35%, and 70% after 60, 90, and 120 min, respectively, ending up with a degradation efficiency of 82% at 150 min., as shown in Fig14(b).

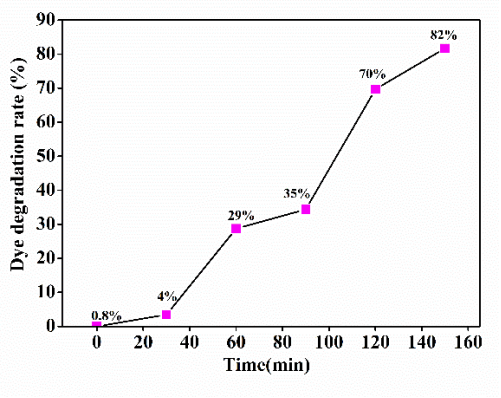
The kinetic analysis of the photodegradation reaction followed the Langmuir-Hinshelwood pseudo first order kinetic (formula), resulting in a rate constant (Kobs) of photocatalytic decomposition of RhB dye estimated at 0.0155 min-1 with a correlation coefficient (R^2) 0.8598.(Fig14(c)), which demonstrate the excellent photo-redox ability of D-CeO_2 NPs to produce reactive oxygen species for the complete mineralization of dyes.



(a)



(b)



(c)

Fig. 14. Photocatalytic activity: (a)Degradation of RhB by D-CeO_2-NPs under UV irradiation (b) Rate constant calculated for the dye degradation reaction following a pseudo-first order (c) Percentage dye degradation rate.

3.2.10 Antimicrobial Assay of CeO_2 NPs.

3.2.10.1 Antibacterial Activity

The synthesized D-CeO_2 NPs were evaluated for their in vitro antibacterial activity against selected *E. Coli* (gram negative) and *S. aureus* (gram positive) bacterial strains using the broth microdilution method. Antibacterial activity was studied by measuring the change in optical density (OD) at 630 nm for different concentrations (0.15-100 µg/mL) of D-CeO_2 NPs. The effect of the concentration of D-CeO_2 NPs on the growth of the two bacterial strains as shown in Fig. 15(a) and Table 6 for *E. coli*, and Fig. 15(b) and Table 7 for *S. aureus*. Turbidity was used as a measure of the ability of the bacterial strains to grow in the presence of different concentrations of D-CeO_2 NPs.

The extent of antibacterial response for each bacterial strain was established quantitatively using the fitted concentration-dependent turbidity readings based on the Gompertz growth model to find log MIC. The log MIC values obtained from the analysis were 1.523 and 1.667 for *E. coli* and *S. aureus*, respectively, translating to MICs of 33.34 µg/mL and 46.42 µg/mL, respectively. Comparing the MICs, it was shown that the D-CeO_2 NPs have a more potent antibacterial effect for the Gram-negative than the Gram-positive bacteria, in line with the observations from the trend in the concentration-dependent turbidity readings. This difference in bacterial susceptibility is likely related to the different cell envelope compositions of the two strains.

The antibacterial mechanism of D-CeO_2 NPs attributed to some or all of the synergistic effects brought about by: (1) interactions with the cell envelope; (2) oxidative stress; and (3) cellular homeostasis disruption. The lipopolysaccharide (LPS) outer membrane of Gram-negative *E. coli* was known to affect various surface properties, such as surface charge, permeability and particle interactions; gram-positive *S. aureus* has a multi-layered cell wall comprised of peptidoglycan which affect the penetration of the NPs and access to the membrane. These differences explain the lower MIC of NPs to *E. coli*, but the relationship between cell-envelope architecture and nanoparticle susceptibility was well known to be complicated, depending on particle size, aggregation, surface charge and characteristics of the medium.

Moreover, the antibacterial effects of D-CeO_2 NPs related with the surface defects, such as the oxygen vacancies, and the reversible redox cycling between Ce^{3+} and Ce^{4+}, which affect the surface reactivity of CeO_2 NPs and allow ROS generating or scavenging depending on the conditions of the experiments. ROS overproduction under the experimental conditions causes oxidative stress, membrane lipid peroxidation, increase in membrane permeability and disruption of vital cellular functions, and leakage of intracellular components. The nanoparticles also interact directly with the bacterial membrane leading to membrane destabilization and cell lysing. The synergistic effect of oxidative stress and membrane damage and responsible for the growth suppression of bacteria.

In particular, the relatively low MIC values achieved against both strains underline the strong antibacterial activity of the prepared D-CeO_2 NPs in vitro, as well as showing a higher susceptibility of the *E. coli* strain over the *S. aureus*, and their potential to serve as an antibacterial nanomaterial given their concentration-dependent antibacterial activity.

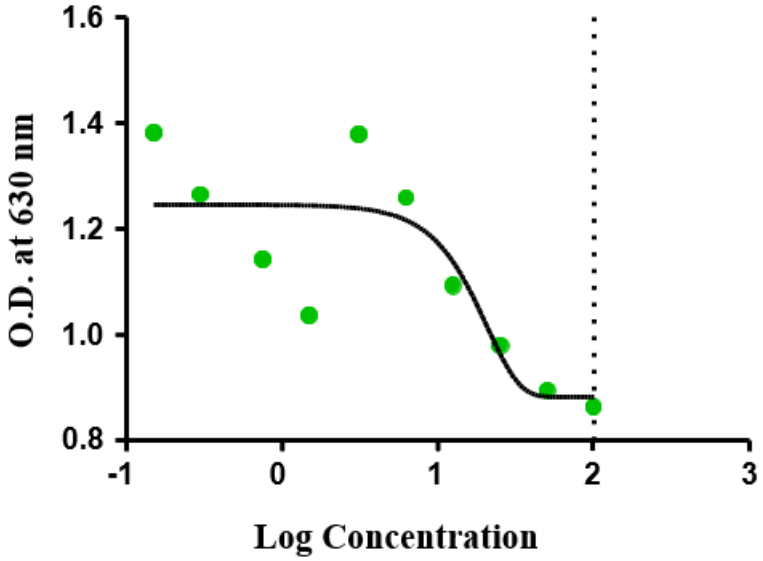
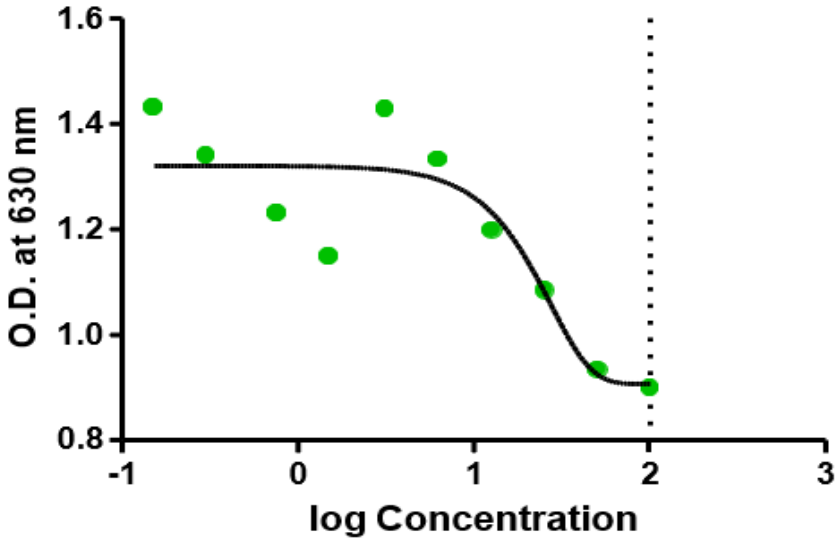


Fig. 15(a). Concentration-dependent (Sigmoidal dose-response) curve of the D-CeO_2 NPs against *E. coli*

Concentrations µg/mL	Log Concentration	O.D. 630 nm
0.15	-0.8239087	1.382
0.3	-0.5228787	1.264
0.75	-0.1249387	1.142
1.5	0.1760913	1.035

3.125	0.49485	1.379
6.25	0.79588	1.258
12.5	1.09691	1.093
25	1.39794	0.978
50	1.69897	0.894
100	2.000	0.862

543 **Table 6.** Experimental data for sigmoidal dose response curve of the D-CeO_2 NPs against *E.*
544 *coli.*



545

546 **Fig. 15(b).** Concentration-dependent (Sigmoidal dose-response) curve of the D-CeO_2 NPs
547 against *S. aureus.*

Concentrations µg/mL	Log Concentration	O.D. 630 nm
0.15	-0.8239087	1.434
0.3	-0.5228787	1.341
0.75	-0.1249387	1.231
1.5	0.1760913	1.149
3.125	0.49485	1.430
6.25	0.79588	1.334
12.5	1.09691	1.200
25	1.39794	1.086
50	1.69897	0.935

100	2.000	0.901

548 **Table 7.** Experimental data for sigmoidal dose response curve of the D-CeO_2 NPs against *S.*
549 *aureus.*

550 **3.2.10.2 Antifungal Activity**

551 The enhanced in vitro antifungal activity of the biosynthesized D-CeO_2 NPs was
552 performed against *A. niger* and *C. albicans* following the agar well diffusion method. The
553 results were subjected to the measurement of the diameter of the inhibition zone around the
554 well containing different doses of the NPs. Fig. 16 shows the antifungal activity of the
555 synthesized D-CeO_2 NPs against *A. niger* and *C. albicans*. Clear and dose-dependent growth
556 inhibition zones were observed with all strains, displaying the marked inhibition of the
557 myceliation of the filamentous fungi as well as its yeast. The inhibition zone growth was
558 proportionally increased with increased doses of NPs, thereby significantly showing the great
559 inhibitory activity of the prepared nanomaterial.

560 The quantitative data shown in Table 8 further supports the antifungal properties
561 exhibited by the biosynthesized D-CeO_2 NPs. The observed inhibition zone diameters for *C.*
562 *albicans* and *A. niger* increased from 19 to 22 mm and 18 to 22 mm, respectively, with
563 increasing nanoparticle dose from 25 to 100 µL, showing a dose dependent efficacy. Similar
564 studies have also reported an increase in inhibition zone size with increasing nanoparticle dose.
565 The corresponding antibacterial activity was ascribed to the increased availability of
566 nanoparticles which renders them more likely to come in contact with the fungal cell envelope,
567 potentially increasing their contact with the cell envelope, and thereby possibly interfering with
568 cell viability. The activity against both fungal species studied here, it also noteworthy since *A.*
569 *niger* and *C. albicans* were quite different with respect to cellular organization, growth and
570 cell-wall constituents.

571 In addition, the antifungal ability of D-CeO_2 NPs was also compared to that of
572 itraconazole, an antifungal drug. When compared at the maximum dose of nanoparticles tested,
573 the inhibition zone was 22 mm for both fungi, while itraconazole at the maximum dose
574 generated zones measuring 14 and 12 mm, respectively. Thus, within the experimental
575 conditions used, the nanoparticles produced inhibition zones that were 8 mm larger than the
576 corresponding solution zone diameters of itraconazole for *A. niger* and 10 mm larger for *C.*
577 *albicans*. The negative control, dimethyl sulfoxide (DMSO), produced no (NI) zones of
578 inhibition in either case, indicating that the solvent solution produced no measurable antifungal

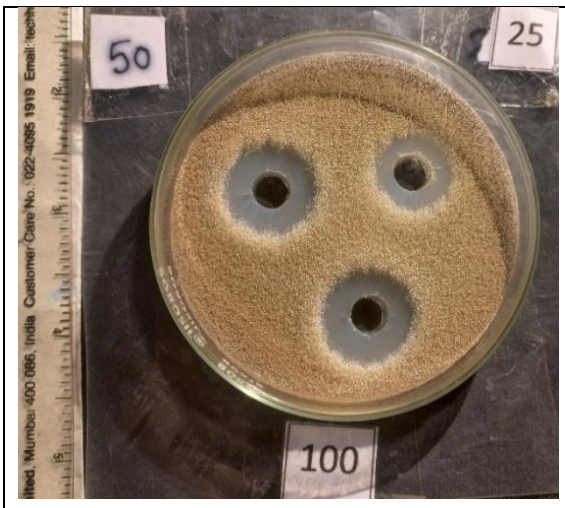
activity at these concentrations. The lack of inhibition with the negative control also rules out the solvent as the cause of the observed inhibitory activity and thereby supports the hypothesis that the nanoparticles are the primary contributing factor. However, for a direct comparison of the antifungal strength, the concentrations, masses, and diffusion rates of each solution need to be included.

The antifungal activity of D-CeO_2 NPs explained by several possible interactions that might occur when nanoparticles surface interacts with the fungal cell surface, induces oxidative stress, and damages homeostasis. The surface of the fungi cell surface has many different kinds of functional groups, which serve as a fulcrum for electrostatic as well as other physical/chemical interactions with nanomaterials. Based on the surface charge of the nanomaterials and solution conditions, such interactions potentially encourage nanoparticle adherence to the cell wall of fungi, and, at a later stage, would likely promote damage to the membrane. With this disruption to the cell's protective barrier, permeability to nutrients and ions hampered, and homeostasis knocked off-balance, putting a stopper to fungal growth as shown with the agar well diffusion antifungal test.

Additionally, the compounds' antifungal activity altered by the unique surface chemistry of cerium oxide nanoparticles (nanoceria), including the presence of Ce^{3+} and Ce^{4+} oxidation states and the surface oxygen vacancies in the nanomaterial. These features alter the redox behaviour of CeO_2 NPs and their catalytic activity, which influence the production or concentration of reactive oxygen species (ROS). ROS accumulation and oxidative stress induce damage to membrane lipids, lead to alterations in membrane proteomics, and interfere with cell growth. This subsequently causes damage to the integrity of the membrane and results in abnormal intracellular electrolyte regulation and cell damage. Although ergosterol was one of the most abundant structural substances in fungal plasma membranes, there was currently no solid evidence that the direct peroxidation of fungal plasma membrane ergosterol occurs as a part of the synthesis mechanism of the nanoparticles.

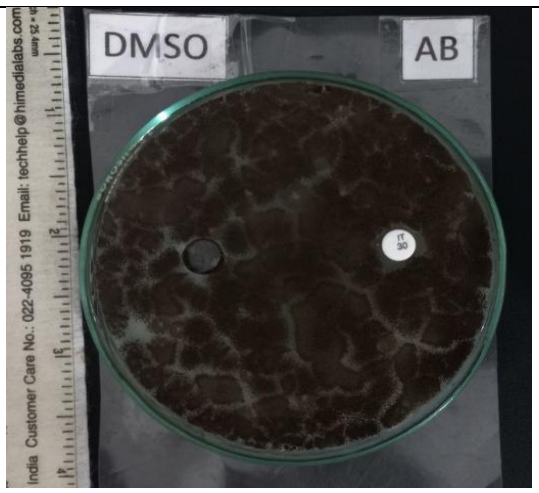
The synergistic effects of nanoparticle-cell-envelope interactions, oxidative stress induction, and suppression of membrane functionality may therefore underpin the remarkable antifungal bioactivity of the D-CeO_2 NPs biosynthesized in this study. The reproducible nature of the inhibition zone formation against both *A. niger* and *C. albicans* isolates, and the escalation of the inhibition-zone diameter on use of the higher nanoparticle dose, reveal the potential of biosynthesized D-CeO_2 NPs as promising antifungal nanomaterials. It is notable that no evidence of inhibition was observed on the DMSO control, suggesting that the observed antifungal activity was related to nanoparticle treatment. These in vitro results suggest that

biosynthesized D-CeO_2 NPs have a promising broad spectrum antifungal effect against the two fungi tested.

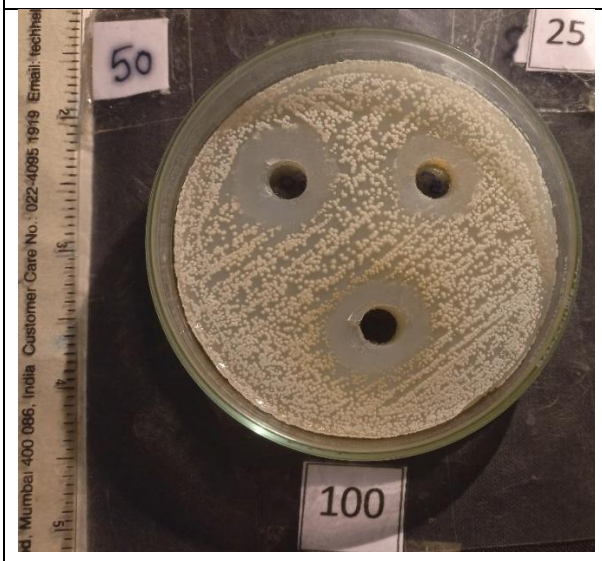


AS14-D-CeO_2-B

D-CeO_2 NPs against ***Aspergillus niger***

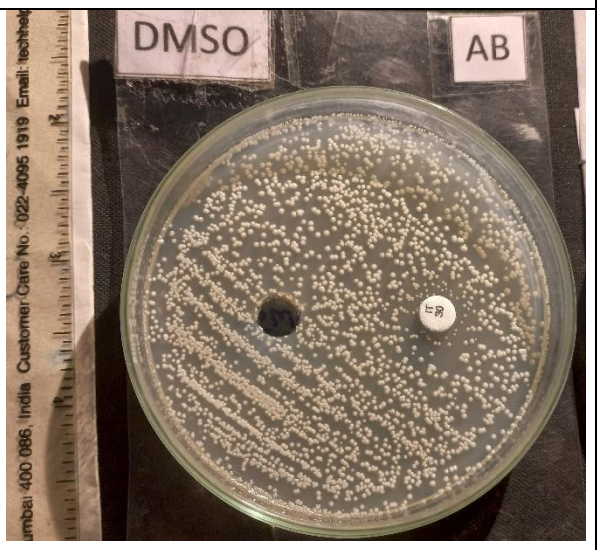


Control against *Aspergillus niger*



CA10-D-CeO_2-B

D-CeO_2 NPs against ***C. albicans***



Control against *C. albicans*

Fig. 16. Antifungal activity of D-CeO_2 NPs displaying zones of inhibition in concentration dependant manner against (a) *A. niger* (AS14) and *(b) C. albicans* (CA10) along with negative control (DMSO) and positive control *(Itraconazole).*

Zone of Inhibition in mm					
Organisms	**25 µL**	**50 µL**	**100 µL**	**Itraconazole**	**DMSO**
AS14-D-CeO_2-B	18	20	22	14	NI

CA10-D-CeO_2-B	19	20	22	12	NI

Table 8. Antifungal activity of D-CeO_2 NPs against *A. Niger* and *C. albicans,* NI-No inhibition.

4. Conclusion

In the current work, a sustainable, economical, and environmental eco-friendly biogenic technique was successfully developed for the green synthesis of cerium oxides nanoparticles (D-CeO_2) employing the aqueous bark extract of *Anogeissus latifolia* as a highly proficient bio reducing and capping agent. The studies carried out by XRD, FT-IR, UV-Vis-NIR, PL, SEM-EDX, HRTEM-SAED, and TG proved the formation of highly thermally stable (up to 800 °C), polycrystalline quasi-spherical nanoparticles with a face cantered cubic fluorite structure having an average crystallite size of 36.73 nm and particle size between 14.59 nm and 69.91 nm. The optical studies have indicated the optical bandgap of 3.0 eV along with a strong defect- related deep-blue photoluminescence with a high degree of color purity (x=0.121, y=0.087) at 469 nm. From functional point of view, the biosynthesized D-CeO_2 NPs exhibited remarkable multifunctional behavior. They served as an excellent heterogeneous photocatalyst with 82% decomposition of Rhodamine B dye within 150 min following Langmuir-Hinshelwood pseudo-first-order kinetics (k=0.0155 min^{-1}, R^2=0.8598), in addition to high antibacterial action against pathogenic bacteria (*E. coli* and *S. aureus*) and fungi (*Aspergillus niger* and *C. albicans*).

The present study confirms the efficacy of biosynthesized D-CeO_2 NPs from novel medicinal plant of *Anogeissus latifolia* for applications in water purification, optoelectronics and medicine.

5. Acknowledgements

The authors are thankful to the Rashtrasant Tukadoji Maharaj Nagpur University, Nagpur for providing Memorial Fellowship (2025–2026) to the first author Mr. Swapnil H. Susundre for a doctoral degree. Also, authors are thankful to the RUSA Centre, RTMNU, Nagpur, Ramdeobaba University, Nagpur, VIT Vellore, STIC Kochi Kerala, India, for providing analysis facilities.

6. Author Contribution

Swapnil H. Susundre: Conceptualization, Data curation, Formal analysis, Investigation, Methodology, Software, Validation, Writing - original draft. **Swapnil R. Mouje:** Writing –

review and editing, and Resources. **Harshal S. Bhoyar:** Software, Formal analysis. **Mayur V. Khedkar:** Project administration, Writing – review and editing. **Shoeb R. Khan:** Conceptualization, Supervision, Validation, Visualization, Writing – review and editing.

7. Declarations

i. Competing Interest

The authors declare no competing interests.

ii. Ethical Approval

Not Applicable.

iii. Funding

None.

8. Data availability

All data generated or analysed during this study is available in this document.

9. References

1. Baig N, Kammakakam I, Falath W. Nanomaterials: a review of synthesis methods, properties, recent progress, and challenges. Mater Adv 2021;2:1821–71. https://doi.org/10.1039/d0ma00807a.
2. Singh KR, Nayak V, Sarkar T, Singh RP. Cerium oxide nanoparticles: properties, biosynthesis and biomedical application. RSC Adv 2020;10:27194–214. https://doi.org/10.1039/d0ra04736h.
3. Charbgoo F, Ahmad M, Darroudi M. Cerium oxide nanoparticles: green synthesis and biological applications. IJN 2017;Volume 12:1401–13. https://doi.org/10.2147/ijn.s124855.
4. Dhall A, Self W. Cerium Oxide Nanoparticles: A Brief Review of Their Synthesis Methods and Biomedical Applications. Antioxidants 2018;7:97. https://doi.org/10.3390/antiox7080097.
5. Rajeshkumar S, Naik P. Synthesis and biomedical applications of Cerium oxide nanoparticles – A Review. Biotechnology Reports 2018;17:1–5. https://doi.org/10.1016/j.btre.2017.11.008.
6. Nosrati H, Heydari M, Khodaei M. Cerium oxide nanoparticles: Synthesis methods and applications in wound healing. Materials Today Bio 2023;23:100823. https://doi.org/10.1016/j.mtbio.2023.100823.

7. Shetty, A. N., S, K., Desai, K. K., & Patil, S. C. (2022). Green Combustion Synthesis of CeO2 Nanostructure Using Aloe vera (L.) Burm f. Leaf Gel and Their Structural, Optical and Antimicrobial Applications. BioNanoScience, 12(3), 757–765. https://doi.org/10.1007/s12668-022-01001-0.
8. Naidi SN, Harunsani MH, Tan AL, Khan MM. Green-synthesized CeO2 nanoparticles for photocatalytic, antimicrobial, antioxidant and cytotoxicity activities. J Mater Chem B 2021;9:5599–620. https://doi.org/10.1039/d1tb00248a.
9. Maqbool Q, Nazar M, Naz S, Hussain T, Jabeen N, Kausar R, et al. antimicrobial potential of green synthesized CeO2 nanoparticles from Olea europaea leaf extract. IJN 2016;Volume 11:5015–25. https://doi.org/10.2147/ijn.s113508.
10. Xu C, Qu X. Cerium oxide nanoparticle: a remarkably versatile rare earth nanomaterial for biological applications. NPG Asia Mater 2014;6:e90–e90. https://doi.org/10.1038/am.2013.88.
11. Wu Y, Ta HT. Different approaches to synthesising cerium oxide nanoparticles and their corresponding physical characteristics, and ROS scavenging and anti-inflammatory capabilities. J Mater Chem B 2021;9:7291–301. https://doi.org/10.1039/d1tb01091c.
12. Singh AK, Bhardwaj K. Mechanistic understanding of green synthesized cerium nanoparticles for the photocatalytic degradation of dyes and antibiotics from aqueous media and antimicrobial efficacy: A review. Environmental Research 2024;246:118001. https://doi.org/10.1016/j.envres.2023.118001.
13. Farias IAP, Santos CCL dos, Sampaio FC. Antimicrobial Activity of Cerium Oxide Nanoparticles on Opportunistic Microorganisms: A Systematic Review. BioMed Research International 2018;2018:1–14. https://doi.org/10.1155/2018/1923606.
14. Kusmierek E. A CeO2 Semiconductor as a Photocatalytic and Photoelectrocatalytic Material for the Remediation of Pollutants in Industrial Wastewater: A Review. Catalysts 2020;10:1435. https://doi.org/10.3390/catal10121435.
15. Matussin SN, Harunsani MH, Khan MM. CeO2 and CeO2-based nanomaterials for photocatalytic, antioxidant and antimicrobial activities. Journal of Rare Earths 2023;41:167–81. https://doi.org/10.1016/j.jre.2022.09.003.
16. Nadeem M, Khan R, Afridi K, Nadhman A, Ullah S, Faisal S, et al.; Green Synthesis of Cerium Oxide Nanoparticles (CeO2 NPs) and Their Antimicrobial Applications: A Review IJN 2020;Volume 15:5951–61. https://doi.org/10.2147/ijn.s255784.

17. Chesneau C, Belbekhouche S. Cerium oxide particles a review: From their synthesis to their physico-chemical characterization, applications to drug delivery field. Powder Technology 2025;464:121167. https://doi.org/10.1016/j.powtec.2025.121167.
18. Kontham S, Mandava K, Dosa S, Mohd FU, Mohammed OA, Mohammad AU. Review on facile synthesis of cerium oxide nanoparticles and their biomedical applications. Inorganic and Nano-Metal Chemistry 2021;52:1183–95. https://doi.org/10.1080/24701556.2021.1963284.
19. Strieder C de M, Macuvele DLP, Soares C, Padoin N, Riella HG. Plant-mediated green synthesis of cerium oxide nanoparticles: A critical perspective of some unclear issues. Journal of Materials Research and Technology 2024;30:6376–88. https://doi.org/10.1016/j.jmrt.2024.05.022.
20. Xu Y, Zhou Y, Li Y, Liu Y, Ding Z. Advances in cerium dioxide nanomaterials: Synthesis strategies, property modulation, and multifunctional applications. Journal of Environmental Chemical Engineering 2024;12:113719. https://doi.org/10.1016/j.jece.2024.113719.
21. Fifere N, Airinei A, Doroftei F, Ardeleanu TS, Dobromir M, Tîmpu D, et al. Phytomediated-Assisted Preparation of Cerium Oxide Nanoparticles Using Plant Extracts and Assessment of Their Structural and Optical Properties. IJMS 2023;24:8917. https://doi.org/10.3390/ijms24108917.
22. Korotkova AM, Borisovna PO, Aleksandrovna GI, Bagdasarovna KD, Vladimirovich BD, Vladimirovich KD, et al. “Green” Synthesis of Cerium Oxide Particles in Water Extracts Petroselinum crispum. CNM 2019;4:176–90. https://doi.org/10.2174/2405461504666190911155421.
23. Dutta D, Mukherjee R, Patra M, Banik M, Dasgupta R, Mukherjee M, et al. Green synthesized cerium oxide nanoparticle: A prospective drug against oxidative harm. Colloids and Surfaces B: Biointerfaces 2016;147:45–53. https://doi.org/10.1016/j.colsurfb.2016.07.045.
24. Aseyd Nezhad S, Es-haghi A, Tabrizi MH. Green synthesis of cerium oxide nanoparticle using Origanum majorana L. leaf extract, its characterization and biological activities. Applied Organom Chemis 2019;34. https://doi.org/10.1002/aoc.5314.
25. Manimaran R. Optimization of Azadirachta indica leaf extract mediated cerium oxide nanoparticles synthesis, characterization, and its applications. Industrial Crops and Products 2023;204:117304. https://doi.org/10.1016/j.indcrop.2023.117304.

744 26. Mim J, Sultana MstS, Dhar PK, Hasan MdK, Dutta SK. Green mediated synthesis of
745 cerium oxide nanoparticles by using Oroxylum indicum for evaluation of catalytic and
746 biomedical activity. RSC Adv 2024;14:25409–24. https://doi.org/10.1039/d4ra04132a.
747 27. Khan M, Mashwani Z-R, Ikram M, Raja NI, Mohamed AH, Ren G, et al. Efficacy of
748 Green Cerium Oxide Nanoparticles for Potential Therapeutic Applications: Circumstantial
749 Insight on Mechanistic Aspects. Nanomaterials 2022;12:2117.
750 https://doi.org/10.3390/nano12122117.
751 28. Gebre SH, Sendeku MG. New frontiers in the biosynthesis of metal oxide nanoparticles
752 and their environmental applications: an overview. SN Appl Sci 2019;1.
753 https://doi.org/10.1007/s42452-019-0931-4.
754 29. Tanwar SN, Parauha YR, There Y, Swart HC, Dhoble SJ. Plant-Based Biosynthesis of
755 Metal and Metal Oxide Nanoparticles: An Update on Antimicrobial and Anticancer Activity.
756 ChemBioEng Reviews 2024;11. https://doi.org/10.1002/cben.202400012.
757 30. Kumar R, Tanwar B, Sharma V, Hajam YA. Botany, traditional uses, phytochemistry,
758 and pharmacological profile of Anogeissus latifolia (Roxb. Ex Dc) Wall. a review. Discov
759 Plants 2025;2. https://doi.org/10.1007/s44372-025-00112-8.
760 31. Khan S, Ahsan F, Mahmood T, Bano S. Anogeissus Latifolia : A Comprehensive
761 Review from Ethanobotanical Insights to Future Pharmacological Frontiers. Chemistry
762 &Amp; Biodiversity 2024;21. https://doi.org/10.1002/cbdv.202401378.
763 32. Govindarajan R, Vijayakumar M, Singh M, Rao ChV, Shirwaikar A, Rawat AKS, et al.
764 Antiulcer and antimicrobial activity of Anogeissus latifolia. Journal of Ethnopharmacology
765 2006;106:57–61. https://doi.org/10.1016/j.jep.2005.12.002.
766 33. Abedi Tameh F, Mohamed HEA, Aghababaee L, Akbari M, Javadi MH, Aucamp M, et
767 al. Characterization and cytotoxicity of nanoceria phytosynthesized using Eucalyptus
768 camaldulensis bark extract. Inorganic Chemistry Communications 2025;178:114576.
769 https://doi.org/10.1016/j.inoche.2025.114576.
770 34. Muthuvel A, Jothibas M, Mohana V, Manoharan C. Green synthesis of cerium oxide
771 nanoparticles using Calotropis procera flower extract and their photocatalytic degradation
772 and antibacterial activity. Inorganic Chemistry Communications 2020;119:108086.
773 https://doi.org/10.1016/j.inoche.2020.108086.
774 35. Hasan N, Wazir NN, Samsudin MY, Syahmi Mohd Sanizam MM, Ahmad NM, Badrol
775 Hisham NA, et al. Evaluation of phytoactive contents and antibacterial activities of green
776 synthesised cerium oxide nanoparticles using Melastoma sp. leaf extract as the capping
777 agent. Heliyon 2024;10:e34558. https://doi.org/10.1016/j.heliyon.2024.e34558.

36. Makarov VV, Love AJ, Sinitsyna OV, Makarova SS, Yaminsky IV, Taliansky ME, et al. “Green” Nanotechnologies: Synthesis of Metal Nanoparticles Using Plants. Acta Naturae 2014;6:35–44. https://doi.org/10.32607/20758251-2014-6-1-35-44.
37. Mestres G, Kugiejko K, Pastorino D, Unosson J, Öhman C, Karlsson Ott M, et al. Changes in the drug release pattern of fresh and set simvastatin-loaded brushite cement. Materials Science and Engineering: C 2016;58:88–96. https://doi.org/10.1016/j.msec.2015.08.016.
38. Teo V, Toh MR, Kwan YH, Raaj S, Tan S-YD, Tan JZY. Association between Total Daily Doses with duration of hospitalization among readmitted patients in a multi-ethnic Asian population. Saudi Pharmaceutical Journal 2015;23:388–96. https://doi.org/10.1016/j.jsps.2015.01.013.
39. Arakha M, Saleem M, Mallick BC, Jha S. The effects of interfacial potential on antimicrobial propensity of ZnO nanoparticle. Sci Rep 2015;5. https://doi.org/10.1038/srep09578.
40. Lam TV, Tran GT, Nguyen NTT, Phan N-K-N, Nguyen DTC. Recent advances in biological, photocatalytic and adsorption applications of biosynthesized CeO2 nanoparticles. Nanoscale Adv 2025;7:7459–82. https://doi.org/10.1039/d5na00876j.
41. Arunachalam T, Karpagasundaram M, Rajarathinam N. Ultrasound assisted green synthesis of cerium oxide nanoparticles using Prosopis juliflora leaf extract and their structural, optical and antibacterial properties. Materials Science-Poland 2017;35:791–8. https://doi.org/10.1515/msp-2017-0104.
42. Marslin G, Siram K, Maqbool Q, Selvakesavan RK, Kruszka D, Kachlicki P, et al. Secondary Metabolites in the Green Synthesis of Metallic Nanoparticles. Materials 2018;11:940. https://doi.org/10.3390/ma11060940.
43. Endo D, Kono T, Koike Y, Yamada J, Maheswari Rajagopalan U. Laser speckle imaging in discrimination of zooplanktons from supermicroplastics. Environmental Nanotechnology, Monitoring & Management 2021;16:100587. https://doi.org/10.1016/j.enmm.2021.100587.
44. Hu H, Zhong Y, Wu H-Y, Huang P, Su Z-M. A new polyniobotungstate based on {GeW9Nb3O40} clusters and nickel cation with photocatalytic properties. Inorganic Chemistry Communications 2020;120:108151. https://doi.org/10.1016/j.inoche.2020.108151.
45. Zhang C, Huang B, Xu J, Cao W, Sun G, Xiao J, et al. Effect of Mo on tribological behaviors of atmospheric plasma sprayed Al2O3-13%TiO2/Mo coatings under boundary

lubrication condition. Ceramics International 2020;46:15066–75. https://doi.org/10.1016/j.ceramint.2020.03.041.

46. Gautam RK, Gautam PK, Banerjee S, Soni S, Singh SK, Chattopadhyaya MC. Removal of Ni(II) by magnetic nanoparticles. Journal of Molecular Liquids 2015;204:60–9. https://doi.org/10.1016/j.molliq.2015.01.038.

47. Shervedani RK, Yaghoobi F, Bagherzadeh M. Electrocatalytic determination of hydroquinone with Mn+ modified gold-5-amino-2-mercaptobenzimidazole self-assembled monolayer electrodes. JICS 2009;6:104–12. https://doi.org/10.1007/bf03246508.

48. GOVINDASAMY G, PONNUSAMI AB. Facile bio-synthesis of cerium oxide nanoparticles, characterization and their photocatalytic potential in the degradation of real tannery wastewater. J Met Mater Miner 2025;35:e2405. https://doi.org/10.55713/jmmm.v35i4.2405.

49. Kim JW, Jung K, Yim T. Dually-functionalized Ni-rich layered oxides for high-capacity lithium-ion batteries. Journal of Materials Science & Technology 2021;86:70–6. https://doi.org/10.1016/j.jmst.2021.01.037.

50. Pelletier DA, Suresh AK, Holton GA, McKeown CK, Wang W, Gu B, et al. Effects of Engineered Cerium Oxide Nanoparticles on Bacterial Growth and Viability. Appl Environ Microbiol 2010;76:7981–9. https://doi.org/10.1128/aem.00650-10.

51. Pop OL, Mesaros A, Vodnar DC, Suharoschi R, Tăbăran F, Mageruşan L, et al. Cerium Oxide Nanoparticles and Their Efficient Antibacterial Application In Vitro against Gram-Positive and Gram-Negative Pathogens. Nanomaterials 2020;10:1614. https://doi.org/10.3390/nano10081614.

52. Altaf M, Manoharadas S, Zeyad MT. Green synthesis of cerium oxide nanoparticles using Acorus calamus extract and their antibiofilm activity against bacterial pathogens. Microscopy Res &Amp; Technique 2021;84:1638–48. https://doi.org/10.1002/jemt.23724.

53. Komal R, Uzair B, Sajjad S, Butt S, Kanwal A, Ahmed I, et al. Skirmishing MDR strain of Candida albicans by effective antifungal CeO2 nanostructures using Aspergillus terreus and Talaromyces purpurogenus. Mater Res Express 2020;7:055004. https://doi.org/10.1088/2053-1591/ab8ba2.

54. Barker E, Shepherd J, Asencio IO. The Use of Cerium Compounds as Antimicrobials for Biomedical Applications. Molecules 2022;27:2678. https://doi.org/10.3390/molecules27092678.

55. Marzban A, Shakib P, Mirzaei SZ, et al (2023) Preparation of Zinc Oxide Nanoparticles Assisted by Okra Mucilage and Evaluation of its Biological Activities. CDDT 20:. https://doi.org/10.2174/1570163820666221201090006
56. Bauer AW, Kirby WMM, Sherris JC, Turck M (1966) Antibiotic Susceptibility Testing by a Standardized Single Disk Method. American Journal of Clinical Pathology 45:493–496. https://doi.org/10.1093/ajcp/45.4_ts.493
57. Shakib P, Mirzaei SZ, Sharafi Z, et al (2023) Biofabrication of copper oxide nanoparticles mediated with Echium amoenum petal extracts for evaluation of biological functions. Biomass Conv Bioref 14:25651–25661. https://doi.org/10.1007/s13399-023-04796-4
58. S K, Perumal P (2018) Antidiabetic and antioxidant activities of ethanolic extracts of piper betle l. leaves in catfish, clarias gariepinus. Asian J Pharm Clin Res 11:194. https://doi.org/10.22159/ajpcr.2018.v11i3.22393
59. Gayathri T, Logesh Kumar S, Sangavi S, et al (2023) Green synthesis of copper oxide nanoparticles using Carica papaya and their antimicrobial activity. Materials Today: Proceedings. https://doi.org/10.1016/j.matpr.2023.11.136
60. Khalaji AD, Pazhand Z, Kiani K, et al (2020) CuO nanoparticles: preparation, characterization, optical properties, and antibacterial activities. J Mater Sci: Mater Electron 31:11949–11954. https://doi.org/10.1007/s10854-020-03749-1.
61. Ramasamy, V., Mohana, V., & Suresh, G. (2018). Study of Ni:CeO2 nanoparticles for efficient photodegradation of methylene blue by sun light irradiation. Indian Journal of Physics, 92(12), 1601–1612. https://doi.org/10.1007/s12648-018-1246-9
62. Arumugam, A., Karthikeyan, C., Haja Hameed, A. S., Gopinath, K., Gowri, S., & Karthika, V. (2015). Synthesis of cerium oxide nanoparticles using Gloriosa superba L. leaf extract and their structural, optical and antibacterial properties. Materials Science and Engineering: C, 49, 408–415. https://doi.org/10.1016/j.msec.2015.01.042
63. Ahmed, H. E., Iqbal, Y., Aziz, M. H., Atif, M., Batool, Z., Hanif, A., Yaqub, N., Farooq, W. A., Ahmad, S., Fatehmulla, A., & Ahmad, H. (2021). Green Synthesis of CeO2 Nanoparticles from the Abelmoschus esculentus Extract: Evaluation of Antioxidant, Anticancer, Antibacterial, and Wound-Healing Activities. Molecules, 26(15), 4659. https://doi.org/10.3390/molecules26154659
64. Hkiri, K., Elsayed Ahmed Mohamed, H., Ghotekar, S., & Maaza, M. (2024). Green synthesis of cerium oxide nanoparticles using Portulaca oleracea Extract: Photocatalytic

activities. Inorganic Chemistry Communications, 162, 112243. https://doi.org/10.1016/j.inoche.2024.112243

65. Majani, S. S., Singh, P., Kumari, P., Setty, P. B. S., Shivamallu, C., Srinivasa, C., Abass, K. S., Iqbal, M., Amachawadi, R. G., Stupin, V., Silina, E., & Kollur, S. P. (2025). Cerium oxide nanoparticles prepared through Bio-combustion using Ficus carica as effective antioxidant, anticancer and dye degrading agent. Scientific Reports, 15(1). https://doi.org/10.1038/s41598-025-13914-3

Supplementary Files

This is a list of supplementary files associated with this preprint. Click to download.

- SupplementryData.docx